

Simulating aerosol lifecycle impacts on the subtropical stratocumulus-to-cumulus transition using large eddy simulations

Ehsan Erfani^{1,1,1}, Peter N. Blossey^{1,1,1}, Robert Wood^{1,1,1}, Johannes K C Mohrmann^{1,1,1}, Sarah J. Doherty^{1,1,1}, Matthew C Wyant^{1,1,1}, and Kuan-Ting O^{1,1,1}

¹University of Washington

November 30, 2022

Abstract

A Large Eddy Simulation (LES) model that simulates the aerosol lifecycle, including aerosol sources and sinks, was used to study the stratocumulus to cumulus transition (SCT). To initialize, force, and evaluate the LES, we used a combination of reanalysis, satellite, and aircraft data from the Cloud System Evolution in the Trades field campaign in summer 2015 over the Northeast Pacific. The simulations follow two Lagrangian trajectories from initially overcast stratocumulus to the tropical shallow cumulus region near Hawaii. The first trajectory is characterized by an initially clean, well-mixed stratocumulus-topped marine boundary layer (MBL), then continuous MBL deepening and precipitation onset followed by a clear SCT and a consistent reduction of aerosols that ultimately leads to an ultra-clean layer in the upper MBL. The second trajectory is characterized by an initially polluted and decoupled MBL, weak precipitation, and a late SCT. Overall, the LES simulates the general MBL features seen in observations. Sensitivity studies with different aerosol initial and boundary conditions reveal aerosol-induced changes in the transition, and albedo changes are decomposed into the Twomey effect and adjustments of cloud liquid water path and cloud fraction. Impacts on precipitation play a key role in the sensitivity to aerosols: for the first case, runs with enhanced aerosols exhibit distinct changes in microphysics and macrophysics such as enhanced cloud droplet number concentration, reduced precipitation, and delayed SCT. Cloud adjustments are dominant in this case. For the second case, enhancing aerosols does not affect cloud macrophysical properties significantly, and the Twomey effect dominates.

Hosted file

2022jd037258-sup-0001-supporting information si-s01.docx available at <https://authorea.com/users/536574/articles/608959-simulating-aerosol-lifecycle-impacts-on-the-subtropical-stratocumulus-to-cumulus-transition-using-large-eddy-simulations>

Simulating aerosol lifecycle impacts on the subtropical stratocumulus-to-cumulus transition using large-eddy simulations

Ehsan Erfani¹, Peter Blossey¹, Robert Wood¹, Johannes Mohrmann¹, Sarah J. Doherty^{1,2},
Matthew Wyant¹, Kuan-Ting O¹

¹Department of Atmospheric Sciences, University of Washington, Seattle, WA, USA

²Cooperative Institute for Climate, Ocean and Ecosystem Studies, University of Washington, Seattle, WA, USA

Correspondence to: Ehsan Erfani, (Ehsan@nevada.unr.edu)

Key points:

An LES is used to study the response of clouds to initial and boundary aerosol perturbations in two marine stratocumulus to cumulus transition cases.

- Although the interactive aerosol scheme within the LES adds new degrees of freedom, the results agree well with observations.
- Precipitation regulates the sensitivity to aerosols and the relative contributions of cloud adjustments to radiative forcing.

This article has been accepted for publication and undergone full peer review but has not been through the copyediting, typesetting, pagination and proofreading process, which may lead to differences between this version and the [Version of Record](#). Please cite this article as [doi: 10.1029/2022JD037258](https://doi.org/10.1029/2022JD037258).

This article is protected by copyright. All rights reserved.

Abstract

Observed stratocumulus to cumulus transitions (SCT) and their sensitivity to aerosols are studied using a Large-Eddy Simulation (LES) model that simulates the aerosol lifecycle, including aerosol sources and sinks. To initialize, force, and evaluate the LES, we used a combination of reanalysis, satellite, and aircraft data from the 2015 Cloud System Evolution in the Trades field campaign over the Northeast Pacific. The simulations follow two Lagrangian trajectories from initially overcast stratocumulus to the tropical shallow cumulus region near Hawaii.

The first trajectory is characterized by an initially clean, well-mixed stratocumulus-topped marine boundary layer (MBL), then continuous MBL deepening and precipitation onset followed by a clear SCT and a consistent reduction of aerosols that ultimately leads to an ultra-clean layer in the upper MBL. The second trajectory is characterized by an initially polluted and decoupled MBL, weak precipitation, and a late SCT. Overall, the LES simulates the observed general MBL features. Sensitivity studies with different aerosol initial and boundary conditions reveal aerosol-induced changes in the transition, and albedo changes are decomposed into the Twomey effect and adjustments of cloud liquid water path and cloud fraction. Impacts on precipitation play a key role in the sensitivity to aerosols: for the first case, runs with enhanced aerosols exhibit distinct changes in microphysics and macrophysics such as enhanced cloud droplet number concentration, reduced precipitation, and delayed SCT. Cloud adjustments are dominant in this case. For the second case, enhancing aerosols does not affect cloud macrophysical properties significantly, and the Twomey effect dominates.

1 Introduction

Low marine clouds are the most widespread clouds on Earth, and they significantly affect the Earth's radiation balance by strongly reflecting sunlight (Wood, 2012). They are also a main source of uncertainty in cloud feedback across global climate models (Bony and Dufresne, 2005; IPCC, 2013; Zelinka et al., 2017), largely due to the necessary use of physics parameterizations that represent subgrid processes in those models. Stratocumulus (Sc) clouds are the predominant type of low marine cloud over the eastern subtropical oceans where the shallow and often well-mixed marine boundary layer (MBL) lies between cold surface ocean water and a strong capping inversion induced by the strong subsidence of warm and dry air aloft (Bretherton et al. 2004; Wood, 2012).

As Sc clouds are transported westward and equatorward by Trade winds, the warmer ocean water enhances surface latent heat fluxes, making the MBL deeper and promoting a decoupled state, with shallow cumulus (Cu) clouds rising into an Sc layer below the inversion. Enhanced buoyancy within the Sc layer, penetrative entrainment by Cu updrafts, and weakened subsidence above the inversion cause stronger entrainment of dry air from the free troposphere (FT) and the eventual dissipation of the Sc cloud (Krueger et al., 1995; Bretherton and Wyant, 1997; Wyant et al., 1997; Zhou et al. 2015). This phenomenon, called the Sc-to-Cu transition (SCT), has been investigated by numerous studies over the previous decades to understand the underlying microphysical and macrophysical processes and the sensitivity of the transition to effects such as downward longwave radiative fluxes, inversion strength (Sandu and Stevens, 2011) and large-scale subsidence (van der Dussen et al., 2016). It is very challenging for weather and climate models to accurately simulate SCTs because of the complex set of physical mechanisms and feedbacks driving the transition (Hannay et al., 2009; Texeira et al., 2011; Lin et al., 2014; Kubar et al., 2015). Large-Eddy

Simulation (LES) is a useful tool for studying SCTs due to its ability to resolve turbulence and cloud processes in the MBL (Sandu and Stevens, 2011; Berner et al., 2013; Blossey et al., 2013; Yamaguchi and Feingold, 2015; Yamaguchi et al., 2017, hereafter Y17; Blossey et al., 2021, hereafter B21).

Aerosols can significantly alter Sc clouds and SCTs. As explained by the first aerosol indirect effect or Twomey effect (Twomey 1977; Platnick and Twomey, 1994), anthropogenic aerosols cause an increase in cloud droplet number concentration (N_c) and a decrease in cloud droplet size, which enhances cloud albedo when macrophysical cloud properties (e.g. liquid water path (LWP) and cloud fraction (CF)) are unchanged. Albrecht (1989) concluded that the resulting smaller cloud droplets would suppress precipitation since they have lower collision-coalescence efficiency.

However, the changes (known as adjustments) in LWP, CF, precipitation, and entrainment generate complex aerosol-cloud interactions beyond simply precipitation suppression (Stevens and Feingold, 2009; Gryspeerd, et al., 2019; Wood, 2021), and this full set of adjustments can partly or fully offset the Twomey effect on albedo (e.g., Glassmeier et al., 2021). These adjustments in LWP and CF to changes in aerosol can therefore lead to either positive or negative cloud radiative forcing depending on the ambient meteorological and aerosol conditions (Ackerman et al., 2004; Wood, 2007; Wood, 2021). Observational studies have found differences in the relative roles of cloud microphysical (i.e. N_c) and macrophysical (i.e. LWP and CF) responses to aerosol perturbations. For example, while cloud adjustments have been observed to offset a small portion of the Twomey effect over continental regions (Trofimov et al., 2020) and over a marine shipping corridor (Diamond et al., 2020), observations have also shown that in some cases they can fully offset the Twomey effect in ship tracks (Coakley and Walsh, 2002; Chen et al., 2012; Gryspeerd, et al., 2019). A recent study by Christensen et al. (2022) concludes that the total adjustments of

clouds and their importance relative to the Twomey effect are uncertain on the global scale. LES and other such simulations can be of utility for improving our understanding of what processes might be driving the differences in cloud responses, and therefore to improve our understanding of aerosol-cloud interactions and their radiative effect on climate.

Previous studies concluded that precipitation can be an important factor in the occurrence of SCT (Xue et al., 2008; Wood et al., 2011; Yamaguchi and Feingold, 2015), and Zhang et al., (2022) find that in the mean, precipitation changes along the SCT are largely driven by decreasing cloud droplet concentration. Using an LES, Y17 highlighted the impact of precipitation on aerosols since collision-coalescence removes not just cloud droplets but also aerosols, leading to further enhancement of drizzle in the aerosol-depleted clouds. Using aircraft observations, Wood et al., (2018) confirmed this and showed that such removal of aerosols results in the development of ultra-clean layers (UCLs), thin and horizontally extensive layers below the MBL inversion during SCT with unactivated aerosol number concentration less than 10 cm^{-3} in the absence of clouds or N_c less than 10 cm^{-3} in the presence of clouds. As shown in O et al (2018), optically thin veil clouds comprise up to 30% of low cloud cover in regions of low cloud transitions. Veil clouds have been associated with ultra clean layers in observations of CSET (Wood et al., 2018), so a better understanding of the interactions between microphysical and macrophysical processes driving the formation of UCLs in these simulations may also shed light on these clouds that contribute to cloud fraction in these regions.

The desire to understand the factors controlling Sc cloud properties and SCTs has motivated intensive observational field campaigns and LES studies along Lagrangian trajectories. The first Lagrangian measurements of SCTs were conducted using aircraft-based observations during the Atlantic Stratocumulus Transition Experiment (ASTEX) over the northeast Atlantic Ocean in June

1992 (Albrecht et al., 1995). Those observations showed that drizzle and dry air above the inversion are important in Sc breakup during SCTs (Bretherton et al., 1999). A recent field campaign, the Cloud System Evolution in the Trades (CSET), was conducted over the Northeast Pacific in the summer of 2015 (Albrecht et al., 2019; Bretherton et al., 2019). To track the evolution of air masses during CSET, flights used a track-and-resample strategy: a westward flight by the National Science Foundation (NSF)/National Center for Atmospheric Research (NCAR) Gulfstream GV aircraft sampled the MBL and lower FT offshore of California using in-situ and remote sensing instruments to measure microphysical and macrophysical characteristics of aerosols and clouds. Then, the Hybrid Single-Particle Lagrangian Integrated Trajectory (HYSPLIT) model was used to construct multiple quasi-Lagrangian forward trajectories (the trajectories are quasi-Lagrangian because they are based on the wind at the 500 m height to represent MBL air movement; for simplicity, hereafter we call them Lagrangian trajectories). The return flight was then planned to intersect and re-sample the same MBL air parcel two days later near Hawaii.

Mohrmann et al. (2019; hereafter M2019) studied 53 Lagrangian trajectories during CSET using satellite and reanalysis products in addition to the aircraft data. That analysis indicated that the CSET cases were representative of the region's summer-time cloud fraction and inversion strength. They also highlighted two Lagrangian cases for modeling studies: L06, a clean case with an initially well-mixed MBL and a clear SCT; and L10, a polluted case with an initially decoupled MBL and much slower cloud evolution. B21 selected these two cases and conducted LES experiments along Lagrangian trajectories using prescribed N_c . The reason for prescribing N_c was the high spatial and temporal variability in aerosol concentration during CSET (Bretherton et al. 2019) and the absence of aerosol boundary conditions outside of the two aircraft flights. On the

other hand, Y17 demonstrated that an LES with a fixed N_c leads to a slow SCT because, by design, it does not include the drizzle enhancement due to the aerosol removal via the collision-coalescence process.

In this study, we build on B21 and conduct Lagrangian LES experiments that include a treatment of the aerosol lifecycle to explore the aerosol-cloud-precipitation interactions for two well-observed case studies, and we evaluate how these case studies respond to perturbed aerosol initial and boundary conditions. Our LES experiments benefit from a prognostic aerosol model (Berner et al., 2013) that simulates aerosol budget tendencies of a single aerosol mode and predicts N_c . The present research is part of the Marine Cloud Brightening (MCB) project, which studies the potential feasibility and efficacy of climate intervention via the deliberate injections of sea-salt spray into the MBL to hinder global warming by enhancing N_c and consequently cloud albedo. It was shown previously that a 5% absolute increase in low cloud cover would be adequate to counteract the global warming caused by CO₂ doubling (Slingo 1990; Wood 2012). However, the enhancement of aerosols may also affect LWP and cloud fraction depending on the aerosol distribution and ambient meteorological conditions, which could affect the climate impact of such aerosol enhancements. This study aims to evaluate the model through comparisons with in situ and remote sensing observations and to shed light on the mechanisms of cloud albedo response to perturbed aerosols under two distinct sets of ambient meteorological conditions. In Section 2, a description of the observational data and LES experimental design is presented. The simulation results are explained in Section 3. These results are then interpreted to explore SCT by precipitation in Section 4 and the decomposition of aerosol-cloud effects in Section 5. Finally, conclusions are given in Section 6.

2 Data and Methods

2.1 Data

The LES experiments in this study are based on the CSET field campaign, which took place in July and August 2015 over the Northeast Pacific (Albrecht et al., 2019). The simulations follow Lagrangian HYSPLIT trajectories from the subtropical Sc deck region offshore of California to the tropical shallow Cu region near Hawaii (Figure 1). Specifically, they follow the two trajectories constructed by M2019 noted above: L06-Tr2.3 (hereafter L06 for simplicity), as a clean case, and L10-Tr6.0 (hereafter L10) as a polluted case (For each CSET case, multiple trajectories are provided, but in this study we select only one trajectory for each case. Therefore, we denote each trajectory by their case name). These trajectories have been extended to include periods before and after the intersection of the research flights with trajectories L06 and L10. Trajectory L06 was sampled by research flight RF06 and then, two days later, by research flight RF07, while L10 was sampled in a similar manner by RF10 and RF11. In-situ aircraft measurements presented in this study are from a flight leg that descended from the lower FT into the sub-cloud layer during the intersection of the flight with the Lagrangian trajectory. This represents a short sampling time (half an hour or less) but provides valuable information about microphysics and macrophysics of aerosol-cloud interactions. The data from this flight path is presented as a single vertical profile for each intersection with the HYSPLIT trajectory.

Observational and reanalysis data are used for both forcing and verifying the Lagrangian LES. Meteorological and thermodynamic variables are extracted from the European Center for Medium-Range Weather Forecasts (ECMWF) ERA5 reanalysis data (Hersbach et al., 2020). Cloud LWP, CF, and surface and top of atmosphere (TOA) radiative fluxes were obtained from the

Accepted Article

Geostationary Operational Environmental Satellite (GOES; Minnis et al., 2008) retrievals, with a horizontal resolution of 5 km and temporal resolution of 5 minutes (GOES data are available at this temporal resolution, but we interpolate them to the time-step of the trajectories, which is hourly), and from Clouds and the Earth's Radiant Energy System (CERES) – Synoptic TOA and surface fluxes and clouds (SYN) – level 3 product (Doelling et al. 2016) with a horizontal resolution of 1° and temporal resolution of 1 hour. The Special Sensor Microwave Imagers (SSM/I; Wentz et al., 2012) with a maximum occurrence of 8 times per day and band-dependent horizontal resolution (from 15×13 to 69×43 km), and the Advanced Microwave Scanning Radiometer (AMSR; Kawanishi et al., 2003) with a maximum occurrence of 2 times per day and band-dependent horizontal resolution (from 5×3 to 62×35 km), were used as additional sources of observed LWP. In addition, we use precipitation, derived from AMSR 89 GHz brightness temperature for shallow marine clouds, which is available twice daily with a horizontal resolution of 10 km (Eastman et al., 2019), and we use cloud-top height (CTH) retrieved from MODIS, available twice daily with the horizontal resolution of 1° (Eastman et al., 2017). The Modern-Era Retrospective analysis for Research and Applications, Version 2 (MERRA2; Gelaro et al., 2017) reanalysis provides aerosol properties with a horizontal resolution of 0.5°×0.625° and a temporal resolution of 3 hours, as generated from the Goddard Chemistry Aerosol Radiation and Transport (GOCART) model, which assimilates meteorological data and satellite observations. As described in Appendix A, we calculate the accumulation-mode N_a using the MERRA-2 aerosol per-species mass and the MERRA-2 assumed particle size distribution, and the resulting MERRA2 N_a are then calibrated through regression against N_a measurements from all the CSET flight data. To compile satellite and reanalysis datasets along the trajectories, each variable is averaged over a 2°×2° box that is centered over the trajectory at each time. The spread in the SSM/I and AMSR variables is

presented as a standard deviation within that box, whereas the spread in GOES variables is calculated as the range in the averages across five $2^\circ \times 2^\circ$ boxes centered on and around the trajectory at each time.

Here, we define a few terms and variables that will be discussed later. First, SCT is defined as the first time low cloud cover (LCC) drops below 50% and remains below 50% for 24 hours after that or until the end of the simulation (whichever is shorter). This definition excludes purely diurnal LCC fluctuations. Second, the inversion height (Z_{inv}) is calculated as the height where $(\frac{d\theta_l}{dz})(\frac{dRH}{dz})$ is minimized. θ_l is liquid-water potential temperature and RH is relative humidity (B21). Over tropical and subtropical oceans, the use of domain-mean profiles of θ_l alone might not be sufficient to detect the inversion at the MBL top when the inversion is weak as, for example, in the trades. In those cases, the inclusion of the mean RH profile was found to help identify the trade inversion due to the strong gradient between the MBL and FT caused by the entrainment of FT dry air to the humid MBL (Dai et al., 2014).

Finally, the entrainment rate (w_e) is calculated as: $w_e = (dZ_{inv}/dt) - w_{ls,inv}$ where dZ_{inv}/dt is the tendency of Z_{inv} , and $w_{ls,inv}$ is the large-scale vertical velocity at Z_{inv} (B21). Although this calculation is an approximation, the resulting residual in the aerosol number budget is a few percent of the dominant terms, and therefore it is accepted and used for stratocumulus clouds (e.g. Berner et al., 2013; B21).

2.1 Model

We use the System for Atmospheric Modeling (SAM; Khairoutdinov and Randall, 2003) version 6.10.9 to conduct the LES experiments. Our simulations with SAM use the Morrison et al. (2005)

microphysics without ice phase hydrometeors or processes, the Rapid Radiative Transfer Model for Global Climate Models (RRTMG; Mlawer et al. 1997), and cloud optical parameterizations from the Community Atmosphere Model version 5 (CAM5; Neale et al. 2010). Berner et al. (2013) coupled the Morrison microphysics to a single-mode bulk (log-normal) aerosol scheme that predicts the mass and number mixing ratios of the accumulation mode aerosol in three categories: unactivated, within-cloud-droplet, and within-rain-drop, by calculating tendencies due to activation, coalescence scavenging (accretion), autoconversion, interstitial scavenging, surface sources, and sedimentation. The reader is referred to Berner et al. (2013) for details on the calculation of each aerosol budget term.

The present simulations include two changes from Berner et al (2013). First, the combined number and mass mixing ratios of unactivated and within-cloud-droplet aerosol (N_a and q_a , respectively) are chosen as prognostic variables rather than the number and mass mixing ratios of unactivated aerosol. The number mixing ratio of unactivated aerosol is computed as the difference between N_a and N_c , and the mass mixing ratio of unactivated aerosol is diagnosed from the combined lognormal size distribution of unactivated and within-cloud-droplet aerosol assuming that the unactivated aerosol occupies the small tail of the size distribution. Note the assumption that each cloud droplet contains exactly one aerosol particle. This method is similar to Wyant et al. (2022), but they used two modes (Aitken and accumulation), whereas we use a single accumulation mode. Second, while the surface flux of aerosol number is unchanged from Berner et al (2013), the surface flux of aerosol mass is corrected to have a characteristic geometric mean dry diameter of 220 nm.

The simulations are performed along L06 and L10, starting at ~ 0.75 days before the westward flight intersection (start time is 17 July 2015, 01Z for L06 and 27 July 2015, 00Z for L10), and

they are run until ~1 day after the return flight intersection, for a total simulation time of ~3.75 days. The number of vertical levels is 432, with the highest resolution (10 m) from 950 m to 3800 m to better capture the complex processes during the evolution of the MBL top. Outside of this range, the vertical grid spacing increases gradually, so it is 25 m near the surface and 60 m below the model top. The horizontal resolution is 100 m for all the simulations. Two horizontal domain sizes are used: $9.6 \times 9.6 \text{ km}^2$ for a total of 12 runs, and $25.6 \times 25.6 \text{ km}^2$ (denoted LD for larger domain) for a total of 4 runs (Table 1). The LES simulations are forced with sea surface temperature (SST) (Fig. 1), geostrophic winds, large-scale vertical velocity (W), and large-scale horizontal advection of temperature and moisture from the ERA5 reanalysis (Fig. 1 in B21). Note that the trajectory is computed based on the velocity at a single height, so wind shear can lead the large-scale advective tendencies to be non-zero away from that height. Initial profiles of temperature and moisture are based on aircraft data in the MBL and ERA5 data aloft, with a blending between the two in the lower free troposphere. See B21 for details. From the initialization time until the time of the westward flight intersection, the horizontally-averaged temperature and total water mixing ratio profiles are nudged to the aircraft profiles on a 3-hour time scale to allow the LES to develop a cloud-topped well-mixed MBL by the time of the westward flight arrival, but after that time, the temperature, moisture, and aerosol within the MBL evolve freely, without any nudging. Throughout the simulation, the temperature, moisture, and aerosol profiles in the free troposphere are also nudged towards a combination of observations and reanalysis starting 500 m above the inversion. A weak nudging of the winds is applied: throughout the simulation, the domain-averaged winds are nudged to ERA5 profiles on a 12-hour time scale. See B21 for more details on the LES configurations.

For each trajectory, one LES simulation is conducted with aerosols prescribed based on in situ observations at the time of the first research flights, so that the LES would simulate realistic initial N_c . In the simulation labeled L06 40-40, the FT and initial MBL N_a are identical at 40 mg^{-1} , while L10 250-60 has initial MBL $N_a=250 \text{ mg}^{-1}$ and FT set to $N_a=60 \text{ mg}^{-1}$ throughout the simulation. Note that each run is labeled by its initial MBL N_a and FT N_a in that order. In other runs, N_a is varied to test the sensitivity of the LES simulations to perturbations in the MBL and FT aerosols. See Table 1 for a full list of simulations. While the FT N_a in the LES is relaxed to these prescribed values throughout the simulation starting 500 m above the inversion, the aerosols within the MBL are allowed to evolve freely so that rapid changes in N_a and N_c , as seen in Y17, can be captured. In addition to simulations with these prescribed two-layer aerosol profiles based on in-situ observations, we also conduct simulations using time-varying vertical profiles of N_a from MERRA2 to initialize the MBL N_a and force the FT N_a in order to develop a framework for running LES purely based on reanalysis products in the absence of any aircraft observations. These profiles, which are computed using the method in Appendix A, are shown in Figure 2 along with in situ observations of N_a from the research flights. Although MERRA2 captures the general features of the aircraft N_a measurements, significant biases exist at certain times and heights. Further comparison of MERRA2 and in-situ N_a is provided in Appendix A (Figure A1). Nonetheless, the MERRA2 aerosols can provide a useful constraint on N_a in remote locations when no aircraft measurements are available.

3 Results

For each L06 or L10 case, a run is selected as the reference and its evolution and comparison with observations are described in more detail. Then, various runs are compared and the sensitivity to

aerosol concentration and domain size is explained. A reference run for each case is selected from the larger-domain runs, using the run that simulates MBL N_a and N_c closest to that from the aircraft and GOES observations at the time of westward aircraft. Based on this criterion, the reference run is 40-40-LD for case L06 (as seen in Figures 3a&b and Figures 4a&b) and 250-60-LD for case L10 (Section 3.2). By studying the reference run for each case, we investigate if the reference run is able to simulate a realistic evolution of N_a and N_c and whether it can estimate the meteorological features similar to observations.

3.1 L06 Case

3.1.1 Reference Run (40-40-LD)

This run is initialized with clean MBL and FT conditions and simulates a consistent reduction of MBL-averaged aerosol and cloud droplet number concentrations (e.g. $\langle N_a \rangle$ and $\langle N_c \rangle$) (Figs. 3a&b) (The MBL-average of each variable is calculated as a density-weighted average of that variable from surface to inversion height (Z_{inv}): $\langle A(t) \rangle = \frac{\int_0^{Z_{inv}} A(z,t)\rho(z,t)dz}{\int_0^{Z_{inv}} \rho(z,t)dz}$, where z is height, t is time, and ρ is air density). This ultimately leads to the formation of a UCL at the top of MBL at the time of the return flight intersection (Figs. 4a&b), in agreement with aircraft aerosol observations and also the observational analysis of Wood et al. (2018). This is a successful test of SAM when using the prognostic bulk aerosol model (B21 used prescribed values of N_c in its simulations, and therefore the ability of SAM to simulate UCL could not be tested). The UCL formation is explored in more detail in Section 4.

The trend of decreasing simulated $\langle N_a \rangle$ along the trajectory is similar to that seen in the aircraft-based observations. Although $\langle N_a \rangle$ from the MERRA2 reanalysis decreases with time, its

concentrations are twice the in-situ $\langle N_a \rangle$ at the time of the initial flight and three times larger than the in-situ measured $\langle N_a \rangle$ at the time of the return flight (Fig. 3a). The reduction in simulated $\langle N_c \rangle$ along the trajectory seems to occur slightly faster than in the aircraft observations, but at a similar rate as in GOES retrievals, albeit with less diurnal variation (Fig. 3b). The GOES retrievals lie within the range of aircraft-derived $\langle N_c \rangle$.

Figures 3d-f illustrate the time series of MBL-averaged aerosol budget tendencies of N_a (In this study, budget tendencies include the total effect of un-activated aerosols, cloud droplets and rain drops). Here, scavenging is the summation of accretion, autoconversion, and interstitial scavenging. For the reference run, the accretion term is 3-4 times stronger on average than autoconversion and interstitial scavenging terms, with the latter two terms having comparable values (This is generally true for all the runs). The sedimentation term is not shown, because its column-averaged values are negligible. For the reference run, the entrainment term is small, because the aerosol gradient between the MBL and FT is negligible initially. By the time this gradient increases the clouds have mostly dissipated and therefore entrainment remains weak after the second night. Scavenging is a stronger sink, causing decreases in $\langle N_a \rangle$ and $\langle N_c \rangle$ that contribute to precipitation onset right before the second night (Fig. 5b). The surface is a strong source of aerosol in the first 12 hours of all runs because the surface winds are strong (figure not shown). This counteracts the accretion sink and leads to a slight increase in $\langle N_a \rangle$ and $\langle N_c \rangle$ over the first night.

The L06 40-40-LD reference run simulates the general observed trend towards the SCT as quantified by comparing the domain-averaged LCC from the simulations and as retrieved from GOES (Fig. 5a). However, it has an overall underestimation in LCC from GOES on the first simulated day. In addition, the simulated SCT onset is early by about half a day, leading to an LCC

underestimation up to the time of return flight observations (day 2.75), suggesting that the positive precipitation-aerosol-scavenging feedback in the prognostic aerosol scheme might be too strong. The LES differs from the observations in not recovering the stratocumulus decks at night once daytime LCC drops below ~50%, whereas the observed clouds make the transition more slowly. As noted later in this Section, the prognostic aerosol scheme used in these runs can lead to a rapid decrease in N_c with the onset of precipitation. This may be driving the more rapid transition in the simulations than is observed.

The underestimation in LCC is also reflected in the comparison of the SW CRE (defined as all-sky minus clear-sky net SW at TOA) (Fig. 3c): although the simulated SW CRE from the reference run weakens from day one to day three, the CERES retrieval of SW CRE on day two is stronger than that simulated, due to earlier cloud breakup in the simulation (In this study, cloud breakup refers to the reduction of domain-averaged LCC from 80% to 20%). The simulated accumulated surface precipitation (Fig. 5b) for L06 40-40-LD is 0.5-2 mm less than the AMSR precipitation throughout the simulation but is within the AMSR uncertainty (1 standard deviation). The reference run shows precipitation onset a few hours before the SCT (on the second night) (Fig. 5a) when the cloud droplet effective radius (r_e) exceeds 15 μm (figure not shown). This value is sometimes used as a threshold radius for the production of significant precipitation in marine low clouds (see Masunaga et al., 2002, and references therein). Precipitation continued until the end of the run but is stronger during the night. This is consistent with the clear diurnal cycle of LWP (Fig. 5d), w_e (Fig. 5e), and turbulence (w'^2) (figure not shown): all three are stronger during the night. As will be discussed later, these changes in precipitation are closely related to changes in entrainment and cloud LWP (Blossey et al., 2013 and references therein)

The three LWP observational products (GOES, SSMI, and AMSR) agree well most of the time (Fig. 5d). Although the simulated LWP in the L06 40-40-LD run is generally lower than the observed values (the exceptions are from day 0.5 to day 0.75 and the last few hours of simulations when SSMI and the LES values agree well), it is mostly within the uncertainty range of the SSMI/AMSR values. A general decrease in LWP is apparent during the SCT in both the reference run and the observed products.

The evolution of the simulated Z_{inv} (Fig. 5c) is very similar to that in ERA5 in the first 24 hours of the simulations because of the nudging that occurs until day 0.75. However, due to the early SCT, subsequent MBL deepening in the reference run is slightly slower than in ERA5, leading to an ultimate underestimation Z_{inv} of 700 m relative to ERA5. As a result, the modeled w_e is generally lower than the ERA5 w_e . Although the reference run is biased low relative to the domain-averaged values of GOES and MODIS CTH most of the time, it has better agreement with the 75th percentile GOES CTH, which represents Cu towers after the SCT.

Despite these biases, the outgoing longwave radiation (OLR) in the L06 40-40-LD run agrees well with CERES observations most of the time (Fig. 5f). The TOA albedo agrees well with the CERES-derived albedo (not shown) on the first day, but underestimates the observation after that, due to early SCT and LCC underestimation in this run.

The vertical profiles of observed and modeled relative humidity (RH) are illustrated in Figs. 4c&d at the times of westward and return flights, respectively. The LES runs were nudged toward the aircraft profiles from the start until day 0.75. Still, the LES develops a sharper inversion (e.g. vertical gradient of variables near the inversion is stronger) and slightly moister MBL profiles at the time of the westward flight.

Two days after the nudging ends, the reference run (L06 40-40-LD) successfully simulates the moisture profile in the MBL as observed from the aircraft, with the exception of the MBL top, where LES Z_{inv} is ~ 500 m shallower than aircraft Z_{inv} . This is due to the early SCT that slows down the MBL deepening. The ERA5 profile within the MBL is drier and slightly warmer, compared to aircraft profiles.

Maps of cloud LWP across the model domain demonstrate the evolution of scattered Cu clouds from Sc clouds along the L06 trajectory (Fig. S1). Before the SCT and near the westward flight time, closed cells are dominant across the domain. A day later (after the SCT), a few bigger cells with cores of strong LWP and precipitation exist along with small patches of Cu clouds scattered throughout the domain. This pattern does not change much until the simulation finish time and is also seen at the time of the return flight.

The evolution of MBL height and thermodynamics, and the structure of mesoscale organizations in our reference run are very similar to the LES result of Lx29 from B21 that used the same settings as our reference run (with the exception of using a prescribed N_c and slightly larger domain size, i.e., 29 km) (their Figs. 7-8). However, our reference run shows an earlier and faster SCT (Figs. S2b&c), because the prognostic aerosol scheme in our LES represents the positive precipitation-aerosol-scavenging feedback that leads to a faster decrease in N_c than the prescribed, linear reduction rate of N_c from 40 to 10 mg^{-1} in B21-Lx29 (Fig. S2). The prognostic N_c plays a key role in the SCT: Y17 conducted idealized LES sensitivity experiments based on a composite Lagrangian trajectory over the Northeast Pacific with prognostic and fixed N_c (their Fig. 10) and showed that the SCT does not occur in runs with fixed N_c because the precipitation feedback does not exist in those runs. Overall, the LES experiments of Y17 that include prognostic N_c show the evolution of the SCT in agreement with our results (e.g. a reduction of N_c , a 12-hour cloud breakup,

and precipitation onset; see their Fig. 3). However, their LES displays a sudden decrease in N_c during the SCT and complete shut-down of MBL deepening afterward, neither of which are seen here. The latter might be due to the constant-in-time subsidence in Y17, in contrast to time-varying subsidence with a net ascent at low levels (<1500 m) between westward and return flights in this study.

3.1.2. Effects of Perturbed Aerosol Initial and Boundary Conditions

Several sensitivity simulations have been made with different initial and boundary conditions for aerosol, and these runs are described in Table 1. The runs with enhanced N_a (e.g. MERRA, MERRA-LD, and MERRAx3) exhibit distinct changes in microphysics and macrophysics. An increase in initial N_a among the different runs leads to enhanced N_c and therefore smaller r_e (figure not shown), which then results in a suppression of the aerosol scavenging term (Fig. 3e). Consequently, enhanced N_a and N_c are associated with stronger entrainment, deeper MBLs, increased turbulence, delayed precipitation onset, reduced accumulated precipitation, and ultimately a delayed SCT (Fig. 5). This is consistent with the LES study of Goren et al. (2019) and the observational study of Christensen et al. (2020), which also found that aerosols prolong cloud lifetime and increase cloud albedo, causing a delay in SCT. The Lagrangian LES runs by Y17 and B21 also are consistent with our study in terms of the sensitivity to N_c . Also, Sandu and Stevens (2011) did an LES sensitivity study wherein they decreased N_c from 100 to 33 cm^{-3} and found that the increased precipitation in the latter run hastens the SCT considerably (their Fig. 8). This agrees with the delay in the SCT with increased N_a and N_c and suppressed precipitation seen here. Although MERRA-LD simulates the timing of SCT more accurately compared to the

reference run, this is achieved at the expense of biased aerosols both at the initial time and during the run.

Using an LES, Sandu et al. (2008) concluded that increased aerosols also produce stronger turbulence and therefore a more well-mixed MBL, which causes stronger entrainment and MBL deepening. Moreover, perturbing N_c seems to modify entrainment through precipitation: by removing liquid water from the entrainment zone, precipitation acts to restrict entrainment, making it difficult to cool and moisten FT air and incorporate it into the MBL. Therefore, runs with enhanced N_c , and suppressed precipitation also have larger Z_{inv} (Albrecht, 1993; Stevens and Seifert, 2008; Blossey et al, 2013).

With a strong N_a gradient between the MBL and FT, the entrainment term in the N_a budget becomes important, as seen in the MERRAx3 run with high MBL N_a (Fig. 3d). A pollution layer (possibly smoke) was transported above the inversion in the MERRA2 reanalysis dataset on day 2 (Fig. 2a), but this is too late in the LES simulation to significantly impact the simulated MBL aerosol concentrations. This is because, despite a strong N_a gradient at the inversion level at the time of return flight for the MERRA and MERRA-LD runs (Fig. 4b), the entrainment becomes negligible after the inversion cloud breakup and precipitation onset (Fig. 3d).

The initial FT N_a has an important role in controlling the MBL N_c , as a large FT N_a increases the MBL N_c through the enhanced entrainment of FT aerosols into the MBL when still in the Sc cloud regime. This addition of aerosols from the FT can be sufficient to counter the loss of MBL aerosol by scavenging processes, as simulated by the 40-150 run (time-series not shown, but mean values are presented in Fig. 10). However, increasing FT N_a later in the simulation, as in the 40-40to150 run, has little impact in this case, and the clouds evolve very similarly to those in the 40-40 run.

Unlike in the reference run, LES runs with a larger initial N_a simulate precipitation onset despite having r_e much smaller than $15\ \mu\text{m}$ (figure not shown). This was previously explained by Wood et al. (2009) (their Fig. A3): with high values of N_c and LWP, there is no need for r_e to exceed the value of $15\ \mu\text{m}$ for precipitation onset.

At the time of the westward flight, the RH profiles of various LES runs are all almost identical (Fig. 4c) because of nudging to aircraft profiles. However, at the time of return flight (Fig. 4d), runs with enhanced N_a have larger Z_{inv} , reflecting the influence of precipitation on inversion height (Albrecht, 1993). The increased entrainment in these runs is also associated with stronger MBL decoupling and a drier MBL.

3.1.3. Effects of Domain Size

Here, we compare two larger-domain runs (40-40-LD and MERRA-LD) with their smaller-domain counterparts (40-40 and MERRA). Looking at 40-40-LD and 40-40, the effect of domain size is modest for a number of metrics: number concentrations time series ($\langle N_a \rangle$ and $\langle N_c \rangle$; Figs. 3a-b), RH profiles (Fig. 4), precipitation onset (Fig. 5c), and SCT initiation onset (Fig. 5a). However, 40-40-LD does exhibit a stronger accretion sink (Fig. 3e) and stronger precipitation on the second night. Furthermore, MBL deepening (Fig. 5c) is slower in 40-40-LD on the second night, and therefore, w_e is smaller (Fig. 5e). Two days into the run, when the SCT has occurred (LCC $\sim 20\%$), the two runs become almost identical until the end of the simulation.

The effect of domain size is more pronounced in runs initialized and forced with higher aerosol concentrations (MERRA-LD and MERRA runs). In these runs, $\langle N_a \rangle$ and $\langle N_c \rangle$ are more than twice that measured from the aircraft at the time of westward flight, but the rate of aerosol

reduction in MERRA-LD is faster so that $\langle N_a \rangle$ and $\langle N_c \rangle$ in the MERRA-LD run are half of that in the smaller-domain MERRA run, and very close to that from the observations, at the time of return flight (Fig. 3a&b). The vertical profiles of $\langle N_a \rangle$ and $\langle N_c \rangle$ reveal that the MERRA-LD run has UCLs at the time of the return flight (Fig. 4a&b). This change in aerosol tendencies seems to be related to precipitation: stronger accretion in MERRA-LD over the first two days leads to earlier precipitation onset and cloud breakup (by about 12 hours) when compared to the MERRA run. At the end of the simulation, accumulated precipitation in MERRA-LD is 25% larger than that in the MERRA run (Fig. 5b). An earlier SCT in the MERRA-LD run leads to lower albedo and smaller w_e , resulting in shallower Z_{inv} . The earlier occurrence of an SCT in simulations with larger domains was also reported in previous studies (e.g. Y17; B21).

Differences in the evolution of cloud morphology in the smaller- and larger-domain MERRA runs play a role in the different SCT timing (Fig. 6). Mesoscale organization quickly emerges in the MERRA-LD run (Fig. 6m). The MERRA run cannot simulate the mesoscale structure due to its small domain size. This is also reflected in the Probability distribution functions (PDFs) of cloud LWP and N_c (Figs. 6a&h) from the two runs, which are broader for MERRA-LD, with higher probability of larger LWP and smaller N_c in MERRA-LD compared with the MERRA run. Overall, a positive feedback is implied: the early broadening at the upper end of the LWP PDF in MERRA-LD run (Figs. 6a&b) is associated with precipitation initiation in larger LWP bins on days 0.5 and 1, and this drives the scavenging of aerosols (Figs. 6e&f). The resulting clean MBL facilitates further precipitation formation, leading to onset of the SCT, when the broadening intensifies for both the LWP and $\langle N_c \rangle$ PDFs, along with the significant increase in precipitation on day 2 of the run (Figs. 6c&g&o). The broadening of PDFs in the MERRA run is negligible until day 2 which is a few hours before SCT.

3.2 L10 Case

3.2.1 Reference Run (250-60-LD)

This case is characterized by an initially polluted MBL. Based on Figs. 7a&b, we selected 250-60-LD as the reference run, because it is the larger-domain run that simulates MBL N_a and N_c closest to the observations. The reference run simulates the overall trend of decreasing $\langle N_a \rangle$ and $\langle N_c \rangle$ over the Lagrangian trajectory, though the rate of reduction in $\langle N_c \rangle$ is slower than in the observations. The modeled $\langle N_c \rangle$ agrees quite well with GOES $\langle N_c \rangle$ on the first day, and the difference with GOES $\langle N_c \rangle$ does not exceed 50% on the second and third days. Uncertainties in instantaneous satellite estimates of N_c are likely to exceed 80% (Grosvenor et al., 2018), which is the approximate difference between the observed N_c values from the aircraft and satellite. As such, the observed and LES N_c values agree to within measurement uncertainty.

The rate of reduction in $\langle N_a \rangle$ and $\langle N_c \rangle$ is insufficient to form a UCL in the reference run, nor is a UCL seen in the aircraft data (Figs. 8a&b). This is in contrast with the L06 case, where an initially cleaner MBL leads to a UCL (Figs. 4a&b). Looking at N_a , the reference run lies within the range of observations in the subcloud layer at the time of both flights (Fig. 8a&b) but underestimates the aircraft observations within the cloud layer at the time of westward flight (day 0.67). At the time of return flight, it under-estimates the aircraft N_a in the lower part of the cloud layer but overestimates N_a and N_c just below the inversion.

The time series of MBL-averaged aerosol budget tendencies of N_a (Figs. 7d-f) for the reference run demonstrates that the scavenging term (with the largest contribution from accretion) is a strong

sink in the first and last 18 hours of the simulation, and its enhancement later in the simulation corresponds to non-negligible precipitation (Fig. 9b). Initially, the entrainment term is a strong aerosol sink in the reference run due to the aerosol gradient between the MBL and FT, but as the MBL N_a decreases with time, so does the MBL-FT gradient; therefore, the entrainment term becomes negligible towards the end of the run. Similar to the L06 case, the surface flux of aerosol in L10 is maximized at the beginning of the simulation, but it is more than five times weaker than the L06 case due to weaker surface winds.

The vertical profile of modeled RH (Fig. 8c) is similar to the aircraft profile at the time of westward flight due to the nudging of the simulation but is slightly moister than aircraft below the Sc cloud layer. At the time of return flight (Fig. 8d), the modeled MBL is slightly drier and deeper than seen by the aircraft.

At the time of the return flight, RH values observed from the aircraft are high (50-90%) above the inversion (Fig. 8d), consistent with the advection of moisture from an adjacent convective system. However, this moist layer is absent in the ERA5 profiles at this time, with RH values much lower (less than 50%) above the inversion for ERA5 and the reference run (which is nudged to ERA5 starting 500m above the inversion).

The evolution of Z_{inv} (Fig. 9c) shows that the reference run under-predicts the inversion height relative to that from ERA5 in the first 24 hours of the simulations, then a deeper MBL after this. The modeled MBL deepens gradually after day 2.3, but the ERA5 MBL shows negligible deepening until day 3.2, and then it suddenly grows over a few hours, due to the moisture advection from an adjacent convective system. The result is that the modeled and ERA5 Z_{inv} are close at the end of the simulation. The reference run underestimates the mean values of GOES CTH from the

westward flight time until about 18 hours later, and overestimates that from day 2.0 until the end of simulation. Kubar et al. (2020) showed that observed CTH and Z_{inv} from satellite retrievals are very similar in the Sc region, but Z_{inv} is higher than CTH in the Cu region because some Cu clouds do not reach the inversion level.

The 250-60-LD reference run presents a strong diurnal cycle as seen by cloud breakup, reduced LWP, and enhanced OLR during the daytime, and vice versa during the nighttime for the first 60 hours of simulation (Figs. 9a&d&f). Observations exhibit a weaker diurnal cycle: GOES shows overcast conditions on the first day and a delayed cloud breakup on the second day (Fig. 9a). As a result of this discrepancy, the reference run overestimates the daytime CERES OLR and underestimates the daytime SW CRE (Fig. 7c) in that time range. Both model and GOES LCC exhibit overcast conditions on the third day, and therefore modeled and CERES OLR and SW CRE agree relatively well. On the last night, the reference run has a stronger cloud breakup than GOES. This coincides with precipitation onset (Fig. 9b), followed by a reduction in LWP (Fig. 9d) and entrainment rate (Fig. 9f) showing the occurrence of SCT in this run (For the reference run, we do not have 24 hours of simulation after the cloud breakup to show that LCC remains below 50%. However, the late cloud breakup occurs during the night and right after precipitation onset and this is different than day-time cloud breakups that has no precipitation. Therefore, we can say with good confidence that the last instance of cloud breakup for the reference run is SCT).

The horizontal distribution of LWP (Fig. S1) demonstrates an overcast Sc layer during the spin-up (day 0.6), followed by the emergence of closed cells as seen on days 1.6 and 2.6. On day 3.6 and after the SCT, the Sc layer has dissipated and a combination of a few bigger cells and smaller patches of Cu exists within the domain. The reference run generally under-predicts LWP relative to GOES, with the two agreeing only for a few hours before the SCT late in the daytime on

simulation day 3. Since the GOES LWP observations are only available for daytime, it isn't possible to test for model bias in LWP relative to GOES during the following nighttime. The modeled LWP is also generally smaller than SSMI and AMSR LWP during the daytime and larger than those during the nighttime (with the exception of the second night), but agrees well with those products in some instances of early morning and early night (e.g. around days 0.7, 2.5, 3.0 and, following the SCT, on day 3.6). The AMSR accumulated precipitation (Fig. 9b) shows that weak precipitation exists at all times over the trajectory, but stronger precipitation is seen in the first and last 12 hours. The 250-60-LD is only able to capture the observed signal in the last 12 hours. Ultimately, the reference run underestimates the AMSR precipitation by 2 mm.

In order to understand the effect of interactive aerosols vs. prescribed N_c , we compare our reference run, 250-60-LD, with the Lx29 run from B21 for the L10 case. Overall, there is good agreement between our reference simulation and the B21-Lx29 for thermodynamic profiles, MBL growth, and the mesoscale organization (figures not shown). Although both studies were initialized with similar aerosols and/or cloud droplet concentrations, the rate of N_c reduction in our reference run is faster than that in B21 in the first 24 hours (Fig. S2d) because an accretion sink (Fig. 7e) and weak precipitation (Fig. 9b) during this time lead to aerosol removal in our reference run.

The two runs have a very similar cloud structure (Figs. S2e&f) until 12 hours before the simulation ends, when the B21-Lx29 simulation demonstrates thinning of Sc clouds, and our reference run shows Sc cloud breakup. Precipitation onset in B21-Lx29 occurs about 12 hours earlier than that in our reference run (figure not shown), however the use of prescribed N_c in B21-Lx29 (a constant value of 60 mg^{-1} in the last 24 hours of simulation) causes a slow reduction of CF. In contrast, the coupled aerosol scheme in our reference run simulates a significant reduction of N_c (e.g. a domain average of about 30 mg^{-1} in the last 24 hrs of the run, and a lower bound marked by standard

deviation reaching to 1 mg^{-1}) prompting cloud breakup. This highlights the advantage of using a prognostic aerosol scheme in LES.

3.2.2. Effects of N_a and N_c

As in L06, the L10 case was simulated with differing aerosol initialization and boundary conditions to understand its sensitivity to aerosol perturbations. Although enhancing N_a in the simulations of L10 (e.g., MERRA, MERRAx3) leads to distinct changes in microphysics [e.g., an increase in N_c (Fig. 7b) and consequent enhancement of cloud optical depth and reduction of τ_e (figures not shown)] and radiation [e.g., enhanced SW CRE (Fig. 7c)], it does not affect meteorological variables significantly. It is only in the last 12 hours of the 3.75-day simulations that the runs show a slight enhancement of Z_{inv} and entrainment rate and reduction of precipitation and OLR with increasing N_a (Fig. 9). Such weak sensitivity of cloud macrophysical properties to N_a in this case is in contrast with the L06 case, and seems to be related to the lack of precipitation-driven diabatic changes due to the higher N_a in the L10 reference case. However, reducing the initial MBL N_a from 250 mg^{-1} to 70 mg^{-1} , as in the 70-60 run, leads to an early reduction in N_c (Fig. 7b) and induces the formation of the UCLs at the time of westward flight (Fig. 8a), consistent with sudden enhancement of scavenging sink (Fig. 7e), precipitation onset and SCT occurrence during the spin-up of this run (Fig. 9). For the rest of simulation, the LWP remains too low to permit the Sc layer restoration, and therefore larger OLR and smaller entrainment rate and Z_{inv} values are seen in this run.

3.2.3. Effects of Domain Size

As in the L06 case, to test for sensitivity to model domain size we developed two pairs of simulations, with each pair was run with identical forcings, but different domain sizes (e.g. 250-

60-LD and 250-60 as the first pair, and 70-60-LD and 70-60 as the second pair). Comparing 250-60-LD and 250-60, the latter does not simulate an SCT (similar to the large and small domain simulations of this case in B21). In fact, the reduction of $\langle N_a \rangle$ and $\langle N_c \rangle$ with time (Figs. 7a&b) is slightly faster in 250-60-LD due to a stronger (albeit still relatively modest) accretion sink (Fig. 6e) and precipitation (Fig. 9b) in the first and last 12 hours of this run. Near the end of this run, the precipitation is strong enough to reduce LWP and cause an SCT, and as a result, 250-60-LD has shallower MBL, larger OLR, and weaker entrainment rate in the last 12 hours. Although precipitation in the L10 case is much weaker than that in the L06 case, the 250-60-LD run accumulates ~3 times more precipitation than the 250-60 run.

Both the 70-60-LD and 70-60 runs simulate an SCT very early on, but the former shows slightly earlier cloud breakup and precipitation onset (Fig. 9) associated with faster reduction of $\langle N_a \rangle$ and $\langle N_c \rangle$ and stronger accretion sink (Fig. 7) in the first 12 hours. After the first day, the two runs are very similar until the end. Ultimately, the 70-60-LD run produces about 25% more accumulated precipitation than the 70-60 run, mainly during the SCT, highlighting the ability of larger domains to support a broader distribution of LWP and precipitation.

Consistent with the L06 case and previous studies (e.g. Y17 and B21), larger-domain runs in the L10 case simulate an earlier occurrence of SCT than the small-domain runs, and this is associated with greater mesoscale organization in the larger-domain runs, as seen in the cloud morphology (Figs. S3m-p) in 250-60-LD after day 2.5. Similar to the L06 MERRA-LD run, a positive feedback exists between cloud LWP, precipitation, and $\langle N_c \rangle$: A broader PDF of LWP leads to stronger precipitation, i.e. more values in larger LWP bins, that consequently remove aerosols and encourage further precipitation, until the SCT in 250-60-LD, when LWP and $\langle N_c \rangle$ PDFs become much broader and precipitation occurs in all LWP bins (Figs. S3a-h).

3.3 Sensitivity of cloud fields to aerosols

Sections 3.1 and 3.2 cover the LES fidelity in representing the cloud fields, which is a primary goal of this study. In this Section, we look at the sensitivity of the results to the aerosol, which is the secondary goal of this study. The domain-averaged time-mean of various microphysical and macrophysical variables as a function of $\langle N_c \rangle$ for all the LES simulations in this study is depicted in Figure 10. Negligible macrophysical sensitivity to $\langle N_c \rangle$ is seen for runs with the mean $\langle N_c \rangle$ larger than $\sim 150 \text{ mg}^{-1}$, as is the case in most of the L10 simulations. Larger $\langle N_c \rangle$ inhibits precipitation and slows the removal of aerosols by autoconversion and accretion, and therefore its further increase has a minimal effect on cloud macrophysical features. This differs from the findings of Xue et al. (2008), who simulated an idealized version of an Atlantic Trade Wind Experiment (ATEX) case that exhibited a decrease in LCC with N_c for N_c greater than 100 mg^{-1} . The LCC decrease in Xue et al. (2008) is not related to precipitation. Instead, the shorter evaporative timescale for small drops is invoked as an explanation: clouds with higher N_c and smaller r_c more readily evaporate. Our LES uses a saturation adjustment approach, and so cannot represent this effect. It does, however, represent the effects of droplet sedimentation (Bretherton et al., 2007) which could, in principle, yield a similar result. More recent LES studies seem to call into question the importance of drop size-dependent evaporation on entrainment rate and cloud macrophysical responses (Williams and Igel, 2021), suggesting that thermal infrared radiative impacts of different drop sizes may be responsible. Such effects are captured in our LES simulations. Thus, it is currently unclear whether we might obtain N_c -induced decreases in LCC in our LES under some meteorological conditions.

Increasing $\langle N_c \rangle$ leads to an enhancement of the short-wave cloud radiative effect (SW CRE; which is equal to all-sky minus clear-sky net SW at TOA) in both trajectories, but as $\langle N_c \rangle$ increases the rate of change in the CRE decreases (Fig. 10a). This is due in part to weaker albedo susceptibility for high $\langle N_c \rangle$ (Platnick and Twomey, 1994; see Sec. 3.5), but the weakening cloud adjustments for $\langle N_c \rangle$ greater than $\sim 100 \text{ mg}^{-1}$ (Figs. 10b&c) are also a major reason.

The decrease in mean precipitation with increasing $\langle N_c \rangle$ in our LES runs (Fig. 10d) is very similar to that given in Fig. 1 in Wood (2005). That study presented a collection of various in situ aircraft and remote sensing observations from different locations around the world, and found that polluted cases (N_c greater than 100 mg^{-1}) correspond to precipitation less than 0.1 mm day^{-1} , whereas clean cases ($N_c \sim 20 \text{ mg}^{-1}$) are associated with precipitation $\sim 1 \text{ mm/day}$.

LWP increases with $\langle N_c \rangle$ when $\langle N_c \rangle$ is less than 100 mg^{-1} (Fig. 10b). This includes all L06 runs, except MERRAx3. For larger $\langle N_c \rangle$, LWP shows a weak decrease with $\langle N_c \rangle$ but remains near 70 g m^{-2} . The majority of L10 runs fall in this regime. This is qualitatively consistent with the behavior seen for precipitating and non-precipitating regimes identified in previous works (e.g. Toll et al. 2017; Hoffmann et al. 2020), though they found a stronger decrease in LWP with $\langle N_c \rangle$ for the non-precipitating regime.

An increase in mean LCC with an increase in mean $\langle N_c \rangle$ for precipitating runs highlights the positive precipitation-aerosol-scavenging feedback, explained in Sections 3.1 and 3.2. Looking at the LCC and precipitation time series for L06, their onset is delayed with the increase in $\langle N_c \rangle$, so that time-mean LCC increases with $\langle N_c \rangle$ (Figs. 5a&b). This is not the case for L10, because there is no SCT and precipitation (except for a few runs, including the reference run), and the LCC does not vary much with $\langle N_c \rangle$.

The partial separation between the L06 and L10 data points in Fig. 10 suggests that meteorological conditions play an important role in the sensitivity of various variables to aerosols. The results of this section are broadly consistent with the LES results of Ackerman et al. (2003), and Ackerman et al. (2004). Although they simulated cases from different field campaigns with different domain sizes and resolutions, they showed that suppressed N_c corresponds to enhanced precipitation, and reduced turbulence and entrainment. Ackerman et al. (2003) showed a strong dependence of LCC, LWP, and precipitation on N_c when N_c falls below 50 cm^{-3} . Similarly, all variables shown in Fig. 10 have stronger sensitivity to N_c for smaller N_c . In addition, the regulation of Z_{inv} by precipitation, as outlined by Albrecht (1993), is evident: the runs with stronger precipitation have shallower MBLs, and the runs with no precipitation have similar Z_{inv} .

4 SCT by precipitation

Feingold and Kreidenweis (2002) noted the efficient removal of aerosol by precipitation for clean cases and called it the “runaway precipitation” process. LES simulations of the transition from closed to open cells by Berner et al. (2013) exhibited similar behavior, followed by suppressed turbulence and entrainment in the resulting low-aerosol MBL. Furthermore, Y17 expressed the importance of precipitation onset in initializing SCT via the “SCT by precipitation” hypothesis. Here, we investigate this in more detail by examining the SCT during two of our LES runs.

Figure 11 presents time-height plots of $\overline{w'^2}$, N_a , CF, and precipitation flux contours before and after SCT for two runs (L06 MERRA-LD and L10 250-60-LD). As a reminder, we define SCT as the first time LCC drops below 50% and remains below 50% for 24 hours after that or until the end of simulation (whichever is shorter). The non-precipitating Sc cloud layer before the SCT has

a thickness of 300-500 m and shows enhanced turbulence (as quantified by $\overline{w'^2}$, which is strongest in the upper half of MBL). The turbulence reaches its peak right before the SCT, associated with convection and formation of Cu clouds (Wood, 2012). This is followed by precipitation onset and a coincident decrease in MBL CF and cloud-layer N_a . The detrainment of air that has been depleted of aerosols by coalescence in a Cu updraft can lead to clouds with low N_c below the inversion (O et al., 2018). Such clouds may precipitate even when LWPs are low, depleting their liquid water content, limiting their ability to cool radiatively, and, possibly, encouraging the breakup of inversion clouds. This is in agreement with Y17 who systematically tested the hypothesis that aerosol removal accelerates precipitation-driven cloud breakup and showed how the N_a gets depleted at the same time as the precipitation enhancement drives the cloud breakup. In contrast, the runs with prescribed N_c in Y17 and B21 simulated much slower SCTs.

The L06 MERRA-LD run produces a UCL, but the near-inversion N_a in the L10 250-60-LD remains larger than 10 mg^{-1} after the SCT. Nevertheless, this is consistent with Fig. 2 in Ackerman et al. (2003), which shows that overcast Sc clouds are unsustainable when N_c falls below about 50 mg^{-1} . Compared to the L06 MERRA-LD run, the inversion cloud breakup in the L10 250-60-LD run is faster and stronger: near-inversion CF values for L06 MERRA-LD remain between 40 and 50% a few hours after the SCT, whereas they drop below 20% for L10 250-60-LD. This seems to be related to the deeper MBL in the latter case. As stated by Eastman and Wood (2016), CF in a shallow precipitating MBL is more persistent than in deep precipitating MBLs. Figures 11g-h depict the vertical profiles of the probability distribution functions of N_a at a few times near the SCT. It is seen that the N_a distribution begins broadening near the inversion about 0.8 days before the SCT. By the time of the SCT, the layer with a broader N_a distribution extends to lower levels,

showing that the ultra-clean layers that first appear near the inversion spread through much of the cloud layer.

For each of the two runs shown in Fig. 11, a time near the SCT with significant surface precipitation is selected and maps of surface precipitation and cloud LWP for the LES domain are displayed in Figs. 12a&b and S4a&b. LWP has local maxima in the cores of mesoscale cells, where strong precipitation occurs. A transect is selected for each map and vertical cross-sections of N_a (non-activated plus within-cloud-droplet aerosol), N_c , rain water mass (q_r), and cloud water mass (q_c) are shown in Figs. 12c&d and S4c&d. In both runs, the remaining Sc clouds (thickness ~ 500 m) and shallow Cu clouds (depth ~ 1500 m) coexist, and precipitation is prevalent in both. The Cu cells contain relatively large N_a and N_c , but UCLs (N_a and $N_c < 10 \text{ mg}^{-1}$) develop near the Cu towers and overall, the near-inversion N_a and N_c remain low ($< 30 \text{ mg}^{-1}$) throughout the transect. These results are in agreement with O et al. (2018), who used an idealized parcel model and showed that the formation of UCLs in the inversion layer is caused by collision-coalescence in the updraft parts of trade Cu, and this diminishes N_c .

Figure S5 shows time-series of cloud cover, cloud LWP, and precipitation for all of the runs from both L06 and L10 that exhibit a clear SCT. Here, time 0 shows the point identified as the SCT for each run. In the two hours before SCT, the LCC and LWP start decreasing rapidly at the same time as the onset of precipitation. During the SCT, the domain-averaged LWP is between 40 and 60 g m^{-2} , and surface precipitation in the Cu cores (quantified as the 95th percentile precipitation) exceeds 20 mm day^{-1} for most runs. Observational studies have shown that marine Sc precipitation at cloud base increases with LWP and decreases with N_c (see Wood, 2012 and references therein). Comstock et al. (2004) and Wood et al. (2011) showed that $\text{LWP} \langle N_c \rangle^{-1}$ is a good indicator of precipitation from satellite data. Our LES runs suggest that $\text{LWP} \langle N_c \rangle^{-1}$ exceeding $\sim 10 \text{ g m}^{-2} \text{ cm}^3$

in the Cu cores can be a predictor of SCT (Fig. S5c). Looking at Fig. 10 in Comstock et al. (2004) and using their power-law relation between LWP N_c^{-1} and precipitation based on radar observations, LWP N_c^{-1} of $10 \text{ g m}^{-2} \text{ cm}^3$ yields precipitation equal to 21.5 mm day^{-1} , which is in rough agreement with the 95th percentile precipitation rate in our LES results (Fig. S5d). Although this value of precipitation is very high for marine low clouds, such values are quite common in pockets of open cells, as shown by in-situ measurements of rain rates in the active and quiescent cells (Fig. 22 in Wood et al., 2011). The results presented here show that the SCT is associated with a reduction of N_a and N_c by precipitation and therefore suggest that aerosol is a key factor in the LES simulations of SCT, and that a transition driven by precipitation is plausible.

5 Decomposing Aerosol-cloud Effects

To gain insights into the relative role of different mechanisms in cloud radiative forcing through aerosols, we separate the cloud radiative effect into that caused by changes in N_c , LWP adjustment, and CF adjustment respectively. We use the N_c effect as our best available approximation of the Twomey effect because it is not possible to accurately calculate the Twomey effect in model experiments with LWP and CF adjustments, since the Twomey effect is defined for fixed LWP and CF.

To calculate each contribution, we assume two states: LES run 1 as the base state, and LES run 2 as the perturbed state. See also Appendix B in Chun et al., (2022). For the first step, we select the base state to be the reference run and the perturbed state to be a run with modified (preferably, enhanced) aerosols. The change in cloud albedo (α_c) due to N_c effect was calculated based on Eq.

(2) in Wood (2021): $\Delta\alpha_c = \frac{\alpha_{c1}(1-\alpha_{c1})(r_N^{1/3}-1)}{1+\alpha_{c1}(r_N^{1/3}-1)}$, where r_N is the ratio of perturbed state cloud

droplet number concentration (N_{c2}) to base state cloud droplet number concentration (N_{c1}) (e.g.

$r_N = \frac{N_{c2}}{N_{c1}}$). α_c can be related to TOA cloudy-sky albedo (A_c) via Eq. (4) in Diamond et al. (2020):

$A_c \approx \alpha_{ft} + \alpha_c \frac{t_{ft}^2}{1 - \alpha_{ft}\alpha_c}$, where α_{ft} is the albedo of the free troposphere (here, it is assumed to be a

constant value of 0.05) and t_{ft} is the transmissivity of the free troposphere and is calculated as

$t_{ft} = \frac{F_{Z_{inv}}^\downarrow}{F_{TOA}^\downarrow}$, where $F_{Z_{inv}}^\downarrow$ is downward SW flux at Z_{inv} and F_{TOA}^\downarrow is solar insolation. Thereafter, the

cloud radiative forcing (ΔR) due to the N_c effect can be calculated based on Eq. (17) in Diamond

et al. (2020): $\Delta R_{N_c} = -C_1 F_{TOA}^\downarrow \Delta A_c$, where C is cloud fraction.

A similar set of equations is used to calculate LWP adjustment, where in this case the $\Delta\alpha_c$ is

calculated as: $\Delta\alpha_c = \frac{\alpha_{c1}(1-\alpha_{c1})(r_L^{5/6}-1)}{1+\alpha_{c1}(r_L^{1/3}-1)}$ where r_L is the ratio of perturbed state LWP (L_2) to base

state LWP (L_1) (e.g. $r_L = \frac{L_2}{L_1}$). Forcing for CF adjustment is calculated as: $\Delta R_{CF} = (C_2 -$

$C_1) F_{TOA}^\downarrow (A_{c2} - A_{clear2})$, where A_{clear} is clear-sky albedo. Finally, we calculate residual forcing

as: $\Delta R_{residual} = \Delta R_{N_c} + \Delta R_{LWP} + \Delta R_{CF} - \Delta R_{LES}$. A small residual is a good indicator of a

successful separation into the three components.

Forcing is non-linear with these properties, so its magnitude will depend on what is chosen as the

“base state”. Therefore, the forcing is calculated in a three-step process:

Step 1: ΔR is calculated with run 1 as the base state and run 2 as the perturbed state (as explained above).

Step 2: ΔR is calculated with run 2 as the base state and run 1 as the perturbed state.

Step 3: ΔR is calculated as the average of the values from steps 1 and 2.

Figure 13 presents ΔA_c and ΔR calculated from the LES simulations as a function of r_N . Shown are changes due to all cloud responses, and the contributions to the total from changes in N_c , LWP, CF, as well as the residual between the sum of these and the total change. ΔA_c and ΔR increase with r_N for both L06 and L10 cases, as does the contribution to ΔA_c and ΔR from the N_c changes, meaning that the stronger the perturbed aerosol concentration, the stronger the cloud albedo and cloud radiative forcing due to the N_c effect. This relationship is similar to the results of Wood (2021; their Fig. 1) for the Twomey effect. Note that the ΔR - r_N relationship for the N_c effect is dependent on both the ΔA_c - r_N relationship for N_c effect (square markers in Fig. 13) and the average change in CF between the pair of runs (figure not shown but can be inferred from Fig. 10).

The LWP adjustment enhances forcing with increasing r_N for L06, but the forcing is reduced with increasing r_N for L10 (as is also evident in the LWP vs. $\langle N_c \rangle$ panel in Fig. 10). The CF adjustment effect is very small for L10, but it is stronger than the N_c effect for L06, consistent with the strong CF sensitivity to $\langle N_c \rangle$ for this case, as shown in Fig. 10. The different behaviors of LWP and CF adjustments between the L06 and L10 cases seem to be related to precipitation: strong precipitation in the L06 case regulates clouds through the removal of aerosols, and the absence of precipitation in the L10 case means this feedback is also absent.

The CF values are very similar between the pairs of L10 LES runs, but the CF evolution differs strongly for the pairs of L06 runs (hence the difference in the length of the error bars for forcing through CF changes in Fig. 13). This also explains why the ΔR values associated with the N_c and LWP effects differ significantly in the two calculations (step 1 versus step 2 above) for L06, but not for L10.

Overall, it is seen that for the clean case (L06) all three effects contribute to the brightening, with the CF adjustment being strongest and LWP adjustment weakest. This highlights the effect of inhibiting the precipitation through enhanced N_c , which leads to increasing CF and LWP (Figs. 14a&c). In contrast, for the polluted case (L10), both ΔA_c and ΔR increase with N_c , and in the absence of negligible CF adjustment (Fig. 14b), a negative LWP adjustment partially offsets the Twomey effect (Fig. 14d). Ultimately, cloud brightening from the increase in N_c dominates for L10. The negative LWP adjustment seems to be due to the continuation of MBL deepening and decoupling in the absence of strong precipitation, which leads to evaporation of near-inversion cloud liquid via entrainment (Ackerman et al., 2004; Xue et al., 2008).

6 Conclusions

Lagrangian LES experiments were developed and conducted along two subtropical MBL air mass trajectories taken from the CSET field campaign (L06 and L10) in order to assess the ability of the LES to reproduce the observed cloud evolution, and in particular to study the role of aerosol-cloud interactions during the SCT. The LES results were evaluated against reanalysis, satellite, and in-situ measurements. The LES used in this study includes a prognostic aerosol model that simulates aerosol budget tendencies and provides a tool to test aerosol removal by precipitation (Wood et al. 2018) and SCT by precipitation (Y17). It also allows quantification of the roles of different processes in two-way aerosol-cloud interactions.

For each of the two cases studied here, a “baseline” run was conducted that used initial aerosol concentrations in the MBL and lower free troposphere that most closely matched those observed from aircraft-based observations during CSET. The LES-simulated characteristics of cloud

evolution in the baseline L06 case are in general agreement with the observations. This is a clean case, with both the model and observations showing a well-mixed Sc-topped MBL on the first day, continuous MBL deepening, and precipitation onset after the first day followed by a clear SCT and formation of UCLs. The simulated SCT occurs slightly earlier than in the observations, and therefore the MBL is shallower. The LES simulates the cloud evolution in the L10 case with somewhat less fidelity. This is a polluted case with a decoupled MBL and, in the simulations, a strong diurnal cycle in LCC. Based on LES, the MBL deepening intensifies after the second day and precipitation onset, and SCT occurs only in the last 12 hours. Observations show slower MBL deepening and continuous, but weak, precipitation throughout the simulation period.

Compared to previous studies with prescribed N_c (e.g. B21), the use of interactive aerosols in our LES experiments adds new degrees of freedom, which makes it more challenging to reproduce the observed trends. For example, changes in aerosol could lead to changes in SW CRE and precipitation through changes in N_c . Feedbacks of precipitation on aerosol through droplet coalescence could amplify biases in precipitation and cloud cover if the aerosol concentration was biased low and clouds were precipitating. These new degrees of freedom result in a simulated SCT that occurs over a shorter time scale, due to the feedbacks of precipitation formation on aerosol concentrations. Nonetheless, these simulations are promising as they compare reasonably well with observations. Capturing a strong two-way feedback between aerosols and precipitation in the L06 case highlights the importance and challenges of including interactive aerosols. Furthermore, the use of interactive aerosols in the model allows for diagnosing the relative roles of various processes in driving aerosol concentration changes and providing guidance on useful metrics for comparisons to other models and observations. The importance of uncertain parameterizations of droplet coalescence during precipitation formation would affect the strength of aerosol feedbacks

on precipitation, so we can expect different warm cloud microphysical parameterizations to produce different precipitation-aerosol-scavenging feedback strengths and different SCT timings when initialized with identical aerosol initial conditions.

The sensitivity of the LES runs to aerosols is strongly dependent on the presence of precipitation and on the aerosol concentration both within and above the MBL. For the clean, precipitating L06 baseline case, enhancement of MBL N_a (either through a larger initial MBL N_a or through the entrainment of N_a from FT) leads to larger N_c , increased LWP, suppressed precipitation, and delayed SCT. Aerosols impact on cloud variables is more significant for runs with smaller N_a because precipitation change with aerosols is stronger for smaller N_a (Figure 10). However, for the polluted, weakly-precipitating L10 baseline case, increasing MBL N_a leads to distinct changes in microphysics (e.g., enhancement of N_c and cloud optical depth, and reduction of r_e), but it causes negligible effects on cloud macrophysical properties (Indeed, this case is non-precipitating for the purpose of aerosol sensitivity test, because such test was conducted by enhancing N_a in small-domain runs and they simulated no significant precipitation. The runs with significantly low initial aerosols lead to precipitation).

When the L10 case is run with lower initial aerosol concentrations, the model simulates precipitation and a clear SCT early in the run. Larger-domain runs are conducted for both this case and the precipitating L06 case. These runs are consistent with the hypothesis by Y17 that precipitation is a driver of SCT, as the decrease in inversion-level clouds, N_a , and N_c after the precipitation onset implies that precipitation-induced reduction in aerosols enhances the breakup of inversion cloud and the SCT.

Large-domain simulations have been found to produce precipitation earlier than those in smaller domains as in, for example, Vogel et al. (2016, Fig. 8), despite the two simulations having similar

boundary layer depths. In our Fig. 6, the PDFs of LWP are seen to be broader in the larger domain, and the largest LWPs lead to an earlier onset of precipitation. We interpret the broader LWP PDF as a reflection of mesoscale organization in the large domain, which is restricted in the small domain by its scale. In the large domain, precipitation onset leads to coalescence scavenging of aerosols and lower N_c concentrations than exist in small domain simulations. These lower N_c values can enhance further precipitation formation and coalescence scavenging of aerosol, which we identify as a precipitation-aerosol-scavenging feedback. This feedback is made visible in Fig. 6, where the precipitation in the large domain exceeds that in the small domain once the tail of small column N_c values emerges in Fig. 6f. In the absence of precipitation, the domain-mean properties of large- and small-domain simulations remain comparable and diverge only after precipitation onset, as seen in B21 and this manuscript (Fig. 9). The absence of prognostic aerosol in B21 indicates that precipitation alone impacts LCC and SCT, but Y17 and this paper suggest that this process may be accelerated by the precipitation-aerosol-scavenging feedback in large domain simulations: the mesoscale organization promotes larger LWP values and precipitation formation, which scavenges aerosols, and the resulting cleaner MBL promotes more precipitation formation, causing the SCT onset.

Based on theoretical analyses from previous studies (e.g. Diamond et al., 2020; Wood, 2021), we decomposed the contributions of the Twomey effect and cloud adjustments to albedo and SW CRE. For both the L06 and L10 cases an increase in aerosols relative to the baseline case leads to an increase in the SW CRE due to the Twomey effect. In contrast, both the sign and magnitude of the SW CRE due to cloud adjustments depend strongly on the meteorological conditions (in particular, precipitation) of each case. For the L06 case, the SW CRE due to cloud adjustments reinforces and is much larger than that of the Twomey effect, because the suppressed precipitation

delays the SCT. For the L10 case, the Twomey effect is dominant, with cloud adjustments only moderately offsetting brightening from the increase in N_c . Here, the cloud adjustments are small because the LCC does not change much with an increase in aerosols in this weakly-precipitating polluted case, and the LWP decreases slightly.

The simulation of these two cases provides a framework for initializing and forcing LES using meteorological and aerosol reanalysis data. Here, aircraft data were available as a second source of aerosol and meteorological data. Comparisons of the aircraft and ERA reanalysis show differences in the thermodynamic profile of the MBL. In addition, MERRA aerosols data is a useful tool, but our simulations show the need for a tighter constraint on aerosols in remote regions. While the L06 MERRA run performs reasonably well, it still simulates too high N_a early in the run. The L10 MERRA run suggests an excessive FT N_a . Future work aims to simulate a larger number of different Lagrangian trajectories under different meteorological and background aerosol conditions to examine the extent to which the results presented here can be generalized.

Acknowledgments

This study was primarily supported by NOAA's Climate Program Office Earth's Radiation Budget (ERB) Program, Grant ##NA20OAR4320271, as well as with funding from, Lowercarbon, the Pritzker Innovation Fund, and SilverLining through the Marine Cloud Brightening Project. This work used the Extreme Science and Engineering Discovery Environment (XSEDE), which is supported by National Science Foundation grant number ACI-1548562, with some simulations performed on Bridges2 at the Pittsburgh Supercomputing Center through allocation TG-ATM190002. This publication is partially funded by the Cooperative Institute for Climate, Ocean,

& Ecosystem Studies (CIOCES) under NOAA Cooperative Agreement NA20OAR4320271, Contribution No. 2022-1204. We appreciate three anonymous reviewers for their constructive comments and Philip Rasch, Je-Yun Chun, Michael Diamond, and Kyoungock Choi for discussions on this research that contributed to the improvement of the final results.

Data Availability Statement

Observations and forcing files along the trajectories, model setup scripts, model outputs, and post-processing Python codes needed to reproduce the results in this paper are available on Zenodo repository at <https://doi.org/10.5281/zenodo.7005166> (Erfani et al., 2022). The SAM code is accessible at <https://you.stonybrook.edu/somas/people/faculty/marat-khairoutdinov/sam/> (Khairoutdinov, 2022). CSET campaign data, including in-situ measurements, were provided by NCAR/EOL under the sponsorship of the National Science Foundation and are available at https://data.eol.ucar.edu/master_lists/generated/cset/ (UCAR/NCAR, 2015). ERA5 data is available at <https://doi.org/10.24381/cds.adbb2d47> (Hersbach et al., 2018). MERRA2 data can be obtained from <https://doi.org/10.5067/VJAFPLI1CSIV> (GMAO, 2015). AMSR and SSMI data are accessible at www.remss.com/missions/ (Wentz et al., 2012; 2014). GOES data can be accessed from <https://doi.org/10.25921/Z9JQ-K976> (NOAA, 1994). CERES SYN1deg data were obtained from <https://ceres.larc.nasa.gov/> (NASA, 2016).

Appendix A: Calculation of MERRA2 N_a

Part 1: Extracting N_a from the mass of different aerosol species

MERRA2 aerosol data contains mass mixing ratio for 5 different species: dust, sea salt, organic carbon (OC), black carbon (BC), and sulfate. For each OC and BC species, two different tracers are available: hydrophilic and hydrophobic. Each dust and sea salt species is divided into 5 size bins (Chin et al., 2002). Therefore, a total of 15 different aerosol tracers are provided in MERRA2 data (Table A1), and the total aerosol number concentration (N_a) is given by:

$$N_a = \sum_{t=1}^{15} N_t$$

where N_t is the number concentration for an individual aerosol tracer (in units of cm^{-3}) and is calculated as:

$$N_t = N_v \frac{\rho_a m_t}{\rho_t} \times 10^{12},$$

where ρ_a is air density (in units of kg m^{-3}), m_t is the mass mixing ratio of the tracer (in units of kg kg^{-1}), ρ_t is the density of tracer (in units of kg m^{-3}), and N_v is the number concentration divided by the total volume of that tracer:

$$N_v = \frac{N_0}{V_0},$$

where N_0 is the total number of particles per unit volume (in units of m^{-3}) and is calculated from Eq. (3) in Grainger (2012):

$$N_0 = \int_{r_d}^{r_u} n(r) dr,$$

where r is dry aerosol particle radius (in units of μm), $n(r)$ is the number density distribution (in units of $\text{m}^{-3} \mu\text{m}^{-1}$), r_d is lower radius, r_u is upper radius and V_0 is the total volume of particles per unit volume and is calculated from Eq. (19) in Grainger (2012):

$$V_0 = \int_{r_d}^{r_u} v(r) dr.$$

Here, $v(r)$ is the distribution of particle volume (in units of μm^{-1}) and is calculated as:

$$v(r) = \frac{4}{3} \pi r^3 n(r),$$

assuming spherical aerosol particles (Eq. 18 in Grainger, 2012). Note that each distribution in this study is a truncated distribution bounded by r_d and r_u for that tracer, and the integrations are solved following the composite trapezoidal rule.

For each OC, BC, and sulfate tracer, MERRA-2 assumes a lognormal distribution (Chin et al., 2002) which is calculated following Eq. (29) in Grainger (2012):

$$n(r) = \frac{N_0}{\sqrt{2\pi} \ln(\sigma_g) r} \exp \left\{ -\frac{[\ln(r) - \ln(r_m)]^2}{2[\ln(\sigma_g)]^2} \right\},$$

where r_m is the modal radius and σ_g is the geometric standard deviation of the distribution.

For each dust tracer, with the exception of the smallest bin, a power distribution is assumed (per the MERRA2 FAQ webpage):

$$n(r) = \alpha r^\beta$$

where α and β are the power-law coefficient and exponent, respectively. Here, $\alpha = 1$ and $\beta = -4$. For the smallest dust bin, a special treatment is considered as this bin is broken down into 4 sub-bins. For each sub-bin, a similar power law is applied, but the mass for each sub-bin (m_s) is calculated as $m_s = w_m \times m_t$, where w_m is the mass weight for that sub-bin. w_m determines the contribution of each sub-bin to the total mass mixing ratio of the smallest dust bin. In other words, the summation of mass weights is equal to unity (Table A1).

For each sea-salt tracer, a modified gamma distribution is used (MERRA2 FAQ webpage) and $n(r)$ is calculated following Eq. (2) in Gong (2003):

$$n(r) = r^{-A}(1 + 0.057r^{3.45}) \times 10^{1.607 \exp(-B^2)}$$

Where $A = 4.7(1 + \Theta r)^{-0.017r^{-1.44}}$ and $B = [0.433 - \log(r)]/0.433$ and Θ is a parameter that controls the shape of sub-micron size distribution and is chosen to be equal to 30. All the required parameters to calculate N_a (e.g. r_d , r_u , r_m , ρ_t , w_m , and σ_g) are provided in Table A1, and m_t and ρ_a are extracted from MERRA2 aerosol data files. As a final note, our calculations are for r greater than 50 nm.

Part 2: Calibration of MERRA2 N_a using aircraft-based observations of N_a from CSET

After calculating the MERRA2 total N_a from the mass of tracers in Part 1, we calibrate this N_a using CSET aircraft-based observations of N_a . Data from all CSET flights are used for this process. The accumulation mode aerosol number is calculated by selecting an aerosol diameter greater than 80 nm. Observed N_a is calculated as the median value for each hour of aircraft data.

Then, the MERRA2 N_a is interpolated to the location of the flight data for each hour. The MBL and FT data are separated by selecting the pressure (P) level of 700 hPa as a threshold for lower FT and 850 hPa as a threshold for the top of MBL. For each MBL and FT section, MERRA2 N_a is regressed against the aircraft-based N_a using a power-law fit (or linear fit in log-log space) (Fig. A1). Higher skill is seen for the FT, with a correlation coefficient (R) of the fit equal to 0.67, whereas R is equal to 0.56 in MBL. With the exception of low values of N_a (e.g. less than 3 cm^{-3}), MERRA2 N_a underestimates aircraft N_a , and the underestimation increases with N_a . For example, when the aircraft-based N_a is equal to 1000 cm^{-3} , N_a derived from MERRA2 is about 6 times smaller than that in the MBL and about 3 times smaller than that in the FT. To correct for this bias, the calibrated MERRA2 N_a is calculated as:

$$N_{a\text{calib}} = \begin{cases} \exp(1.43\ln(N_a) - 0.25), & P \geq 700 \text{ hPa} \\ \exp(1.20\ln(N_a) - 0.08), & P \leq 850 \text{ hPa} \end{cases}$$

References

- Ackerman, A.S., Toon, O.B., Stevens, D.E. and Coakley Jr, J.A., 2003: Enhancement of cloud cover and suppression of nocturnal drizzle in stratocumulus polluted by haze. *Geophysical research letters*, 30(7).
- Ackerman, A. S., Kirkpatrick, M. P., Stevens, D. E., and Toon, O. B., 2004: The impact of humidity above stratiform clouds on indirect aerosol climate forcing. *Nature*, 432(7020), 1014-1017.
- Albrecht, B.A., 1989: Aerosols, cloud microphysics, and fractional cloudiness. *Science*, 245(4923), 1227-1230.
- Albrecht, B.A., Bretherton, C.S., Johnson, D., Schubert, W.H. and Frisch, A.S., 1995: The Atlantic stratocumulus transition experiment—ASTEX. *Bulletin of the American Meteorological Society*, 76(6), 889-904.
- Albrecht, B.A., 1993. Effects of precipitation on the thermodynamic structure of the trade wind boundary layer. *Journal of Geophysical Research: Atmospheres*, 98(D4), 7327-7337.

Albrecht, B., V. Ghaté, J. Mohrmann, R. Wood, et al., 2019: Cloud System Evolution in the Trades—CSET

Following the Evolution of Boundary Layer Cloud Systems with the NSF/NCAR GV. *Bull. Amer. Meteor. Soc.*, 100, 93–121, doi: 10.1175/BAMS-D-17-0180.1.

Berner, A. H., C. S. Bretherton, R. Wood, and A. Muhlbauer, 2013: Marine boundary layer cloud regimes and POC formation in an LES coupled to a bulk aerosol scheme. *Atmos. Chem. Phys.*, 13, 12549–12572, <https://doi.org/10.5194/acp-13-12>

Blossey, P.N., Bretherton, C.S., Zhang, M., Cheng, A., Endo, S., Heus, T., Liu, Y., Lock, A.P., de Roode, S.R. and Xu, K.M., 2013. Marine low cloud sensitivity to an idealized climate change: The CGILS LES intercomparison. *Journal of Advances in Modeling Earth Systems*, 5(2), 234–258

Blossey, P. N., C. S. Bretherton, J. Mohrmann, 2021: Simulating observed cloud transitions in the northeast Pacific during CSET. *Mon. Wea. Rev.*, 149(8), 2633–2658, <https://doi.org/10.1175/MWR-D-20-0328.1>

Bony, S. and Dufresne, J.L., 2005: Marine boundary layer clouds at the heart of tropical cloud feedback uncertainties in climate models. *Geophysical Research Letters*, 32(20).

Bretherton, C. S., & Wyant, M. C., 1997: Moisture transport, lower-tropospheric stability, and decoupling of cloud-topped boundary layers. *J. Atmos. Sci.*, 54 (1), 148–167.

Bretherton, C. S., S. K. Krueger, M. C. Wyant, P. Bechtold, E. Van Meijgaard, B. Stevens, and J. Teixeira, 1999: A GCSS boundary-layer cloud model intercomparison study of the first ASTEX Lagrangian experiment. *Bound.-Layer Meteor.*, **93**, 341–380,

Bretherton, C.S., Uttal, T., Fairall, C.W., Yuter, S.E., Weller, R.A., Baumgardner, D., Comstock, K., Wood, R. and Raga, G.B., 2004: The EPIC 2001 stratocumulus study. *Bulletin of the American Meteorological Society*, 85(7), 967–978.

Bretherton, C. S., Blossey, P. N., & Uchida, J., 2007: Cloud droplet sedimentation, entrainment efficiency, and subtropical stratocumulus albedo. *Geophysical research letters*, 34(3), L03813.

Bretherton, C. S., McCoy, I. L., Mohrmann, J., Wood, R., Ghaté, V., Gettelman, A., Bardeen, C. G., Albrecht, B. A., & Zuidema, P. (2019). Cloud, Aerosol, and Boundary Layer Structure across the Northeast Pacific Stratocumulus–Cumulus Transition as Observed during CSET. *Mon. Wea. Rev.*, 147(6), 2083–2103. <https://doi.org/10.1175/MWR-D-18-0281.1>

Chen, Y.-C., Christensen, M. W., Xue, L., Sorooshian, A., Stephens, G. L., Rasmussen, R. M., & Seinfeld, J. H.

(2012). Occurrence of lower cloud albedo in ship tracks. *Atmos. Chem. Phys.*, 12(17), 8223–8235.

Chin, M., P. Ginoux, S. Kinne, O. Torres, B. Holben, B. Duncan, R. Martin, J. Logan, A. Higurashi, and T.

Nakajima, 2002: Tropospheric aerosol optical thickness from the GOCART model and comparisons with satellite and Sun photometer measurements. *J Atmos Sci*, 59-3, 461–483.

Christensen, M. W., et al. 2022.: Opportunistic experiments to constrain aerosol effective radiative forcing, *Atmos. Chem. Phys.*, 22, 641–674.

Chun, J.-Y., Wood, R., Blossey, P., and Doherty, S. J. 2022: Microphysical, macrophysical and radiative responses of subtropical marine clouds to aerosol injections, *Atmos. Chem. Phys. Discuss.*, 351.

Coakley Jr, J. A., & Walsh, C. D. (2002). Limits to the aerosol indirect radiative effect derived from observations of ship tracks. *Journal of the Atmospheric Sciences*, 59(3), 668–680.

Comstock, K. K., Wood, R., Yuter, S. E., & Bretherton, C. S. (2004). Reflectivity and rain rate in and below drizzling stratocumulus. *Quarterly Journal of the Royal Meteorological Society*, 130(603), 2891–2918.

Christensen, M.W., Jones, W.K. and Stier, P., 2020: Aerosols enhance cloud lifetime and brightness along the stratus-to-cumulus transition. *Proceedings of the National Academy of Sciences*, 117(30), 17591-17598.

Dai, C., Wang, Q., Kalogiros, J. A., Lenschow, D. H., Gao, Z., & Zhou, M., 2014: Determining boundary-layer height from aircraft measurements. *Boundary-layer meteorology*, 152(3), 277-302.

Diamond, M. S., Director, H. M., Eastman, R., Possner, A., & Wood, R., 2020: Substantial Cloud Brightening from Shipping in Subtropical Low Clouds. *AGU Advances*, 1, e2019AV000111.

<https://doi.org/10.1029/2019AV000111>.

Doelling, D. R., M. Sun, L. T. Nguyen, M. L. Nordeen, C. O. Haney, D. F. Keyes, and P. E. Mlynchzak, 2016: Advances in geostationary-derived longwave fluxes for the CERES synoptic (SYN1deg) product. *J. Atmos. Oceanic Technol.*, **33** (3), 503–521, doi:10.1175/JTECH-D-15-0147.1.

Eastman, R., & Wood, R., 2016: Factors controlling low-cloud evolution over the eastern subtropical oceans: A Lagrangian perspective using the A-Train satellites. *Journal of the Atmospheric Sciences*, 73(1), 331-351.

Eastman, R., Wood, R. & O, K-T., 2017: The subtropical stratocumulus-topped planetary boundary layer: A climatology and the Lagrangian evolution. *J. Atmos. Sci.*, 74, 2633-2656. <https://doi.org/10.1175/JAS-D-16-0336.1>

Eastman, R., Lebsock, M., & Wood, R., 2019: Warm Rain Rates from AMSR-E 89-GHz Brightness Temperatures Trained Using CloudSat Rain-Rate Observations. *Journal of Atmospheric and Oceanic Technology*, 36(6), 1033–1051.

Erfani, E., P. Blossey, R. Wood, S. Doherty, J. Mohrmann, M. Wyant, K. O., 2022: Data for paper: simulating aerosol lifecycle impacts on the subtropical stratocumulus-to-cumulus transition using large-eddy simulations [Dataset]. Zenodo. <https://doi.org/10.5281/zenodo.7005166>.

Feingold, G. and Kreidenweis, S. M.: Cloud processing of aerosol as modeled by a large eddy simulation with coupled microphysics and aqueous chemistry, *J. Geophys. Res.*, 107, 4687, doi:10.1029/2002JD002054, 2002.

Gelaro, R., McCarty, W., Suárez, M. J., Todling, R., Molod, A., Takacs, L., et al., 2017: The modern-era retrospective analysis for research and applications, version 2 (MERRA-2). *J. Clim.*, 30(14), 5419–5454.

Glassmeier, F., Hoffmann, F., Johnson, J. S., Yamaguchi, T., Carslaw, K. S., & Feingold, G., 2021: 900 Aerosol-cloud-climate cooling overestimated by ship-track data. *Science*, 371(6528), 485–489.
<https://doi.org/10.1126/science.abd3980>.

Global Modeling and Assimilation Office (GMAO) (2015), MERRA-2 3D IAU State, Meteorology Instantaneous 3-hourly (p-coord, 0.625x0.5L42), version 5.12.4, Greenbelt, MD, USA: Goddard Space Flight Center Distributed Active Archive Center (GSFC DAAC), <https://doi.org/10.5067/VJAFPLI1CSIV>. Valid as of 09/20/2022.

Gong, S., 2003: A parameterization of sea-salt aerosol source function for sub- and super-micron particles. *Global Biogeochemical Cycles*, 17(4), 1097.

Goren, T., Kazil, J., Hoffmann, F., Yamaguchi, T., & Feingold, G., 2019: Anthropogenic Air Pollution Delays Marine Stratocumulus Breakup to Open Cells. *Geophysical Research Letters*, 46(23), 14135–14144.
<https://doi.org/10.1029/2019GL085412>.

Grainger, R. G., 2012: Some useful formulae for aerosol size distributions and optical properties. *Lect. Notes (University of Oxford)*, 12-3.

Grosvenor, D. P., et al., 2018: Remote Sensing of Droplet Number Concentration in Warm Clouds: A Review of the Current State of Knowledge and Perspectives. *Reviews of Geophysics*, 56(2), 409–453.
<https://doi.org/10.1029/2017RG000593>.

Gryspeerd, E., Goren, T., Sourdeval, O., Quaas, J., Mülmenstädt, J., Dipu, S., Unglaub, C., Gettelman, A., and Christensen, M., 2019: Constraining the aerosol influence on cloud liquid water path, *Atmos. Chem. Phys.*, 19, 5331–5347.

Hannay, C., Williamson, D.L., Hack, J.J., Kiehl, J.T., Olson, J.G., Klein, S.A., Bretherton, C.S. and Köhler, M., 2009: Evaluation of forecasted southeast Pacific stratocumulus in the NCAR, GFDL, and ECMWF models. *Journal of Climate*, 22(11), 2871-2889.

Hersbach, H., and Coauthors, 2018: ERA5 hourly data from 1959 to present. Copernicus Climate Change Service (C3S) Climate Data Store (CDS). [Dataset]. <https://doi.org/10.24381/cds.adbb2d47>. Valid as of 09/20/2022.

Hersbach, H., and Coauthors, 2020: The ERA5 global reanalysis. *Quart. J. Roy. Meteor. Soc.*, **146 (730)**, 1999–2049, doi:10.1002/qj.3803.

Hoffmann, F., Glassmeier, F., Yamaguchi, T., & Feingold, G., 2020: Liquid Water Path Steady States in Stratocumulus: Insights from Process-Level Emulation and Mixed-Layer Theory. *Journal of the Atmospheric Sciences*, 77(6), 2203–2215. <https://doi.org/10.1175/JAS-D-19-0241.1>

IPCC, 2013: Climate Change 2013: The Physical Science Basis. T. F. Stocker et al., Eds., Cambridge University Press, 1535 pp.

Kawanishi, T., Sezai, T., Ito, Y., Imaoka, K., Takeshima, T., Ishido, Y., Shibata, A., Miura, M., Inahata, H. and

Spencer, R.W., 2003: The Advanced Microwave Scanning Radiometer for the Earth Observing System (AMSR-E), NASDA's contribution to the EOS for global energy and water cycle studies. *IEEE Transactions on Geoscience and Remote Sensing*, 41(2), 184-194.

Khairoutdinov, M. F., and D. A. Randall, 2003: Cloud resolving modeling of the ARM summer 1997 IOP: Model formulation, results, uncertainties, and sensitivities. *J. Atmos. Sci.*, 60 (4), 607–625, doi:10.1175/1520-0469(2003)060<0607:CRMOTA>2.0.CO;2.

Khairoutdinov, M. F., 2022: System for Atmospheric Modeling [Software]. <https://you.stonybrook.edu/somas/people/faculty/marat-khairoutdinov/sam/>.

Krueger, S. K., McLean, G. T., & Fu, Q., 1995: Numerical simulation of the stratus-to-cumulus transition in the subtropical marine boundary layer. part I: Boundary-layer structure. *J. Atmos. Sci.*, 52 (16), 2839-2850.

Kubar, T.L., Stephens, G.L., Lebsock, M., Larson, V.E. and Bogenschutz, P.A., 2015: Regional assessments of low clouds against large-scale stability in CAM5 and CAM-CLUBB using MODIS and ERA-Interim reanalysis data. *Journal of Climate*, 28(4), 1685-1706.

Kubar, T. L., Xie, F., Ao, C. O., & Adhikari, L. (2020). An assessment of PBL heights and low cloud profiles in CAM5 and CAM5- CLUBB over the Southeast Pacific using satellite observations. *Geophysical Research Letters*, 47(2), e2019GL084498.

Lin, J.L., Qian, T. and Shinoda, T., 2014: Stratocumulus clouds in Southeastern Pacific simulated by eight CMIP5–CFMIP global climate models. *Journal of Climate*, 27(8), 3000-3022

Masunaga, H., T. Y. Nakajima, T. Nakajima, M. Kachi, and K. Suzuki (2002), Physical properties of maritime low clouds as retrieved by combined use of TRMM Microwave Imager and Visible/Infrared Scanner: 2.

Climatology of warm clouds and rain, *J. Geophys. Res.*, **107**(D19), 4367, doi:10.1029/2001JD001269.

Minnis, P., and Coauthors, 2008: Near-real time cloud retrievals from operational and research meteorological satellites. *Remote Sensing of Clouds and the Atmosphere XIII*, International Society for Optics and Photonics, Vol. 7107, 710703, doi:10.1117/12.800344.

Mlawer, E.J., Taubman, S.J., Brown, P.D., Iacono, M.J. and Clough, S.A., 1997: Radiative transfer for inhomogeneous atmospheres: RRTM, a validated correlated- k model for the longwave. *Journal of Geophysical Research: Atmospheres*, 102(D14), 16663-16682.

Mohrmann, J., C. S. Bretherton, I. L. McCoy, J. McGibbon, and R. Wood, 2019: Lagrangian evolution of the Northeast Pacific marine boundary layer structure and cloud during CSET. *Mon. Wea. Rev.*, 147, 4681–4700, DOI: 10.1175/MWR-D-19-0053.1.

Morrison, H.C.J.A., Curry, J.A. and Khvorostyanov, V.I., 2005. A new double-moment microphysics parameterization for application in cloud and climate models. Part I: Description. *Journal of the atmospheric sciences*, 62(6), 1665-1677.

NASA, Langley Research Center, 2016: Hourly CERES and geostationary (GEO) TOA fluxes, and Fu-Liou radiative transfer surface and in-atmospheric (profile) fluxes. [Dataset] <https://ceres.larc.nasa.gov/>. Valid as of 09/20/2022.

- Neale, R. B., and Coauthors, 2010: Description of the NCAR Community Atmosphere Model (CAM5.0). NCAR Tech. Note NCAR/TN-4861STR, 268 pp., www.cesm.ucar.edu/models/cesm1.1/cam/docs/description/cam5_desc.pdf.
- NOAA Office of Satellite and Product Operations, 1994: NOAA Geostationary Operational Environmental Satellite (GOES) I-M and N-P Series Imager Data. NOAA National Centers for Environmental Information. [Dataset] doi:10.25921/Z9JQ-K976. Valid as of 09/20/2022.
- O, K., Wood, R., & Bretherton, C. S., 2018: Ultraclean Layers and Optically Thin Clouds in the Stratocumulus-to-Cumulus Transition. Part II: Depletion of Cloud Droplets and Cloud Condensation Nuclei through Collision–Coalescence. *Journal of the Atmospheric Sciences*, 75(5), 1653–1673.
- Platnick, S., & Twomey, S., 1994: Determining the Susceptibility of Cloud Albedo to Changes in Droplet Concentration with the Advanced Very High-Resolution Radiometer. *Journal of Applied Meteorology*, 33(3), 334–347. [https://doi.org/10.1175/1520-0450\(1994\)033<0334:DTSOCA>2.0.CO;2](https://doi.org/10.1175/1520-0450(1994)033<0334:DTSOCA>2.0.CO;2).
- Sandu, I., Brenguier, J.L., Geoffroy, O., Thouron, O. and Masson, V., 2008: Aerosol impacts on the diurnal cycle of marine stratocumulus. *Journal of Atmospheric Sciences*, 65(8), 2705-2718.
- Sandu, I. and Stevens, B., 2011: On the factors modulating the stratocumulus to cumulus transitions. *Journal of Atmospheric Sciences*, 68(9), 1865-1881.
- Stevens, B. and Seifert, A., 2008. Understanding macrophysical outcomes of microphysical choices in simulations of shallow cumulus convection. *Journal of the Meteorological Society of Japan. Ser. II*, 86, pp.143-162.
- Slingo, A., 1990: Sensitivity of the Earth's radiation budget to changes in low clouds. *Nature*, 343(6253), 49-51.
- Stevens, B., Feingold, G., 2009: Untangling aerosol effects on clouds and precipitation in a buffered system. *Nature* **461**, 607–613. <https://doi.org/10.1038/nature08281>
- Teixeira, J., Cardoso, S., Bonazzola, M., Cole, J., DelGenio, A., DeMott, C., Franklin, C., Hannay, C., Jakob, C., Jiao, Y. and Karlsson, J., 2011: Tropical and subtropical cloud transitions in weather and climate prediction models: The GCSS/WGNE Pacific Cross-Section Intercomparison (GPCI). *Journal of Climate*, 24(20), 5223-5256.
- Toll, V., Christensen, M., Gassó, S., & Bellouin, N., 2017: Volcano and ship tracks indicate excessive aerosol-induced cloud water increases in a climate model. *Geophysical Research Letters*, 44, 12,492–12,500. <https://doi.org/10.1002/2017GL075280>.

- Trofimov H, Bellouin N, and Toll V, 2020: Large-Scale Industrial Cloud Perturbations Confirm Bidirectional Cloud Water Responses to Anthropogenic Aerosols, *J. Geophys. Res.-Atmos*, 125, e2020JD032575
- Twomey, S., 1977: The Influence of Pollution on the Shortwave Albedo of Clouds. *J. Atmos. Sci.*, 34, 1149–1152. [https://doi.org/10.1175/1520-0469\(1977\)034<1149:TIOPOT>2.0.CO;2](https://doi.org/10.1175/1520-0469(1977)034<1149:TIOPOT>2.0.CO;2).
- UCAR/NCAR, Earth Observing Laboratory, 2015: Cloud System Evolution over the Trades, UCAR/NCAR [Dataset]. https://data.eol.ucar.edu/master_lists/generated/cset/. Valid as of 09/20/2022.
- Van der Dussen, J.J., De Roode, S.R. and Siebesma, A.P., 2016: How large-scale subsidence affects stratocumulus transitions. *Atmospheric Chemistry and Physics*, 16(2), 691-701
- Vogel R, Nuijens L, Stevens B, 2016: The role of precipitation and spatial organization in the response of trade-wind clouds to warming. *J Adv Model Earth Syst*, 8, 843–862.
- Wentz, F.J., T. Meissner, C. Gentemann, K.A. Hilburn, J. Scott, 2014: Remote Sensing Systems GCOM-W1 AMSR2 Environmental Suite on 0.25 deg grid, Version 7. Remote Sensing Systems, Santa Rosa, CA. [Dataset] www.remss.com/missions/amsr, valid as of 9/20/2022.
- Wentz, F., K. Hilburn, and D. Smith, 2012: Remote Sensing Systems DMSP SSM/I Daily Environmental Suite on 0.25 deg grid, Version 7. Remote Sensing Systems, Santa Rosa, CA. [Dataset] <http://www.remss.com/missions/ssmi/>. valid as of 9/20/2022.
- Williams, A. S., & Igel, A. L., 2021: Cloud Top Radiative Cooling Rate Drives Non-Precipitating Stratiform Cloud Responses to Aerosol Concentration. *Geophysical Research Letters*, 48(18), e2021GL094740. <https://doi.org/10.1029/2021GL094740>.
- Wood, R., 2007: Cancellation of Aerosol Indirect Effects in Marine Stratocumulus through Cloud Thinning. *J. Atmos. Sci.*, 64, 2657–2669. <https://doi.org/10.1175/JAS3942.1>.
- Wood, R., Kubar, T.L. and Hartmann, D.L., 2009: Understanding the importance of microphysics and macrophysics for warm rain in marine low clouds. Part II: Heuristic models of rain formation. *Journal of the Atmospheric Sciences*, 66(10), 2973-2990.
- Wood, R., Bretherton, C.S., Leon, D., Clarke, A.D., Zuidema, P., Allen, G. and Coe, H., 2011: An aircraft case study of the spatial transition from closed to open mesoscale cellular convection over the Southeast Pacific. *Atmospheric Chemistry and Physics*, 11(5), 2341-2370.
- Wood, R., 2012: Stratocumulus clouds. *Monthly Weather Review*, 140(8), 2373-2423.

- Wood, R., O, K.T., Bretherton, C.S., Mohrmann, J., Albrecht, B.A., Zuidema, P., Ghate, V., Schwartz, C., Eloranta, E., Glienke, S. and Shaw, R.A., 2018: Ultraclean layers and optically thin clouds in the stratocumulus to-cumulus transition. Part I: Observations. *J. Atmos. Sci.*, 75 (5), 1631–1652, doi:10.1175/JAS-D-17-0213.1.
- Wood, R., 2021: Assessing the potential efficacy of marine cloud brightening for cooling Earth using a simple heuristic model, *Atmos. Chem. Phys.*, 21, 14507–14533.
- Wyant, M.C., Bretherton, C.S., Rand, H.A. and Stevens, D.E., 1997: Numerical simulations and a conceptual model of the stratocumulus to trade cumulus transition. *Journal of Atmospheric Sciences*, 54(1), 168-192.
- Wyant, M. C., Bretherton, C. S., Wood, R., Blossey, P. N., & McCoy, I. L. (2022). High free-tropospheric Aitken-mode aerosol concentrations buffer cloud droplet concentrations in large-eddy simulations of precipitating stratocumulus. *Journal of Advances in Modeling Earth Systems*, 14, e2021MS002930.
- Xue, H., Feingold, G., & Stevens, B., 2008: Aerosol effects on clouds, precipitation, and the organization of shallow cumulus convection. *Journal of the Atmospheric Sciences*, 65(2), 392-406.
- Yamaguchi, T. and Feingold, G., 2015: On the relationship between open cellular convective cloud patterns and the spatial distribution of precipitation. *Atmospheric Chemistry and Physics*, 15(3), 1237-1251.
- Yamaguchi, T., Feingold, G. and Kazil, J., 2017: Stratocumulus to cumulus transition by drizzle. *Journal of Advances in Modeling Earth Systems*, 9(6), 2333-2349.
- Zelinka, M.D., Randall, D.A., Webb, M.J. and Klein, S.A., 2017: Clearing clouds of uncertainty. *Nature Climate Change*, 7(10), 674-678.
- Zhang, Z., Oreopoulos, L., Lebsock, M. D., Mechem, D. B., & Covert, J. (2022). Understanding the microphysical control and spatial-temporal variability of warm rain probability using CloudSat and MODIS observations. *Geophysical Research Letters*. <https://doi.org/10.1029/2022gl098863>
- Zhou, X., Kollias, P. and Lewis, E.R., 2015: Clouds, precipitation, and marine boundary layer structure during the MAGIC field campaign. *Journal of Climate*, 28(6), 2420-2442.
- Wood, R., 2005: Drizzle in stratiform boundary layer clouds. Part I: Vertical and horizontal structure. *Journal of the atmospheric sciences*, 62(9), 3011-3033.
- MERRA2 FAQ webpage: <https://gmao.gsfc.nasa.gov/reanalysis/MERRA-2/FAQ/>, valid as of 5/20/2022.

Figure Captions

Figure 1. Selected CSET Lagrangian trajectories (filled markers) and flight paths (westward solid cyan lines, eastward dashed cyan lines) for the a) L06 and b) L10 cases used in this study. The filled markers' shades show the evolution in CERES low cloud cover along the trajectories. In the background map, shaded contours, black contours, and vectors show the ERA5 SST, surface pressure, and 10m wind speed, respectively, averaged for the periods a) 17-20 July 2015 and b) 27-30 July 2015.

Figure 2. Time-height evolution of corrected MERRA2 N_a for the a) L06 and b) L10 cases. The superimposed thin vertical rectangles at about days 0.75 and 2.75 show the aircraft measurements of N_a for reference.

Figure 3. Left panels: time series for L06 of observed and modeled domain-averaged a) MBL-average total aerosol number concentration ($\langle N_a \rangle$), b) MBL-average cloud droplet number concentration ($\langle N_c \rangle$), and c) the shortwave cloud radiative effect (SW CRE, calculated as the all-sky minus clear-sky net SW at TOA). Right panels: select MBL-average aerosol budget tendencies for N_a due to d) cloud-top entrainment of lower FT air, e) MBL-averaged scavenging, and f) surface fluxes in units of $\text{mg}^{-1} \text{day}^{-1}$. The light gray boxes show the nighttime periods.

Figure 4. Vertical profiles of the observed and modeled domain-averaged N_a and N_c at the time of the a) westward and b) return flight observations for the L06 case. c&d) as in (a&b), but for relative humidity (RH).

Figure 5. Macrophysical cloud properties for the L06 case from the simulations and observations. Time series of domain-averaged a) low cloud cover (LCC), b) accumulated precipitation, c) inversion height (Z_{inv}), d) cloud liquid water path (LWP), e) entrainment rate (w_e), and f) outgoing longwave radiation (OLR). The light gray boxes show the nighttime periods.

Figure 6. a-d) Probability distribution functions of cloud LWP at four times for L06, MERRA and MERRA-LD runs. The dots show precipitation in bins of LWP, and the boxes on the upper-right corner of each panel show domain-averaged LWP for MERRA (first value) and MERRA-LD (second value). Each panel shows data averaged for a period of 1 hour. e-h) as in a-d, but for $\langle N_c \rangle$.

i-l) Snapshots of cloud LWP at four times for MERRA run. m-p) as in i-l, but for MERRA-LD run.

Figure 7. As in Figure 3, but for the L10 case.

Figure 8. As in Figure 4, but for the L10 case.

Figure 9. As in Figure 5, but for the L10 case.

Figure 10. Microphysical and macrophysical variables as a function of $\langle N_c \rangle$ for the L06 (circles) and L10 (squares) cases, from both the simulations and selected observations. Variables on the y-axis are a) the short-wave cloud radiative effect (SW CRE), b) cloud LWP, c) LCC, d) surface precipitation, e) τ_c , f) r_e , g) Z_{inv} , and h) w_e . Each colored point shows results for one LES run averaged over the whole day-time period of the run. Observed values are plotted as black or gray circles for L06 and black or gray squares for L10 case. Here, the observed values of $\langle N_c \rangle$ are from GOES and the observed or reanalysis values of parameters are from sources as given in the upper-right corner of each panel.

Figure 11. Time-height evolution of a&b) w'^2 , c&d) cloud fraction (CF) and precipitation flux, and e&f) N_a . The x-axis is time in fraction of a day relative to the time of the SCT. G&h) The vertical profiles of N_a are shown at several times near the time of the SCT. For each time, the shaded area between the two lines shows the 5th and 95th percentile range in the variable's probability distribution function (PDF). The results are for two LES runs: L06 MERRA-LD (left panels) and L10 250-60-LD (right panels).

Figure 12. Left panels: snapshots of a) surface precipitation, and b) cloud LWP for the L06 MERRA-LD run at a time close to the SCT, day 1.875 (relative to the run start). Right panels: y-z cross-sections of c) N_a and d) N_c , with contours of rain mass or q_r (1e-4, 1e-3 kg kg⁻¹) and cloud liquid mass or q_c (1e-5, 1e-4, 1e-3 kg kg⁻¹). Cross-sections are at x = 8 km (black lines in the left panels).

Figure 13. Upper panels: change in cloudy-sky albedo (ΔA_c) as a function of the ratio of the perturbed to baseline cloud droplet number concentration ($r_N = \frac{N_{c2}}{N_{c1}}$) for a) L06 and b) L10. Lower panels: change in the cloud radiative effect (ΔR) as a function of r_N for c) L06 and d) L10. Each

point shows the variables for a pair of LES runs with values averaged over the whole day-time period of the run. The filled circles show the total change in A_c and R between the two LES runs. The square, diamond, triangle, and plus markers, respectively, show the effects of changes in N_c , LWP, CF, and the residual ($CDNC + LWP + CF - Total$). The markers for N_c , LWP, CF, and residual show the results of step 3, whereas the endpoints of bars show steps 1 and 2 of the calculations described in the text.

Figure 14. Upper panels: ratio of the perturbed to baseline cloud fraction ($r_C = \frac{C_2}{C_1}$) as a function of the ratio of the perturbed to baseline cloud droplet number concentration ($r_N = \frac{N_{c2}}{N_{c1}}$) for the a) L06 and b) L10 cases. Lower panels: r_N as a function of the ratio of the perturbed to baseline liquid water path ($r_L = \frac{L_2}{L_1}$) for the c) L06 and d) L10 cases. Each point shows the ratio between a pair of LES runs with values averaged over the whole day-time period of the run.

Figure A1. Linear regression in log-log space between N_a from all CSET flights and N_a derived from collocated MERRA2 data.

Figure S1. Snapshots of cloud LWP for the L06, 40-40-LD run on days a) 0.6, b) 1.6, c) 2.6 and d) 3.6 following the start of the simulation. e-h) As in a-d, but for the L10, 250-60 run.

Figure S2. a) Time series of observed and modeled domain-averaged, MBL-averaged $\langle N_c \rangle$ for this study's L06 40-40-LD run and for the L06 Lx29 run from B21. b) Time-height evolution of domain-averaged cloud fraction for this study's L06 40-40-LD run. c) As in b, but for the L06 Lx29 run from B21. d-f) As in a-c, but for this study's L10 250-60-LD run and the L10 Lx29 run from B21.

Figure. S3. As in Fig. 6, but for 250-60 and 250-60-LD runs.

Figure S4. As in Figure 12, but for L10 250-60-LD and for x-z cross-sections at $y = 23$ km (black lines on left panels). Here, the data are for day 3.375 relative to the run start.

Figure. S5. Time series of a) LCC, b) cloud LWP, c) 95th percentile cloud LWP $\langle N_c \rangle^{-1}$, and d) 95th percentile surface precipitation for all the runs with clear SCT. The x-axis is time (in units of day) with SCT selected as 0.

Tables

Table 1. A description of LES runs performed in this study.

Run name	Case	Domain size (km)	Initial MBL N_a (mg^{-1})	FT N_a (mg^{-1})
40-40	L06	9.6×9.6	40	40
40-40to150	L06	9.6×9.6	40	Initial: 40 gradual increase to: 150
150-40	L06	9.6×9.6	150	40
40-150	L06	9.6×9.6	40	150
MERRA	L06	9.6×9.6	MERRA (103)*	MERRA (68)**
MERRAx3	L06	9.6×9.6	MERRAx3 (309)*	MERRA (68)**
40-40-LD	L06	25.6×25.6	40	40
MERRA-LD	L06	25.6×25.6	MERRA (103)*	MERRA (68)**
70-60	L10	9.6×9.6	70	60
110-60	L10	9.6×9.6	110	60
250-60	L10	9.6×9.6	250	60
250-200	L10	9.6×9.6	250	200
MERRA	L10	9.6×9.6	MERRA (215)*	MERRA (270)**
MERRAx3	L10	9.6×9.6	MERRAx3 (645)*	MERRA (270)**
250-60-LD	L10	25.6×25.6	250	60
70-60-LD	L10	25.6×25.6	70	60

* Initial MBL-averaged N_a based on MERRA data

** Time-mean FT value of N_a right above the inversion from MERRA data

Table A1. Various aerosol properties for different tracers available in MERRA2 data. This table is compiled based on the results of Chin et al. (2002) and MERRA2 FAQ webpage.

Aerosol tracer	Size distribution	Density (kg m ⁻³)	Modal radius (μm)	Effective radius (μm)	Lower radius (μm)	Upper radius (μm)	mass weight	Geometric standard deviation (μm)
OC, hydrophilic	Lognormal	1800	0.0212	---	0.1	0.3	---	2.20
OC, hydrophobic	Lognormal	1800	0.0212	---	0.1	0.3	---	2.20
BC, hydrophilic	Lognormal	1800	0.0118	---	0.1	0.3	---	2.00
BC, hydrophobic	Lognormal	1800	0.0118	---	0.1	0.3	---	2.00
Sulfate	Lognormal	1700	0.0695	---	0.1	0.3	---	2.03
Dust, 1	Power special	2500	0.220	0.73	0.10	0.18	0.009	2.00
					0.18	0.3	0.081	
					0.3	0.6	0.234	
Dust, 1	Power special	2500	0.220	0.73	0.6	1.0	0.676	2.00
Dust, 2	Power	2650	0.421	1.4	1.0	1.8	---	2.00
Dust, 3	Power	2650	0.7220	2.4	1.8	3.0	---	2.00
Dust, 4	Power	2650	1.3540	4.5	3.0	6.0	---	2.00
Dust, 5	Power	2650	2.4068	8.0	6.0	10.0	---	2.00
Sea Salt, 1	Modified Gamma	2200	0.023	0.079	0.03	0.1	---	2.03
Sea Salt, 2	Modified Gamma	2200	0.090	0.316	0.1	0.5	---	2.03
Sea Salt, 3	Modified Gamma	2200	0.090	1.119	0.5	1.5	---	2.03
Sea Salt, 4	Modified Gamma	2200	0.805	2.818	1.5	5.0	---	2.03
Sea Salt, 5	Modified Gamma	2200	2.219	7.772	5.0	10.0	---	2.03

Figures

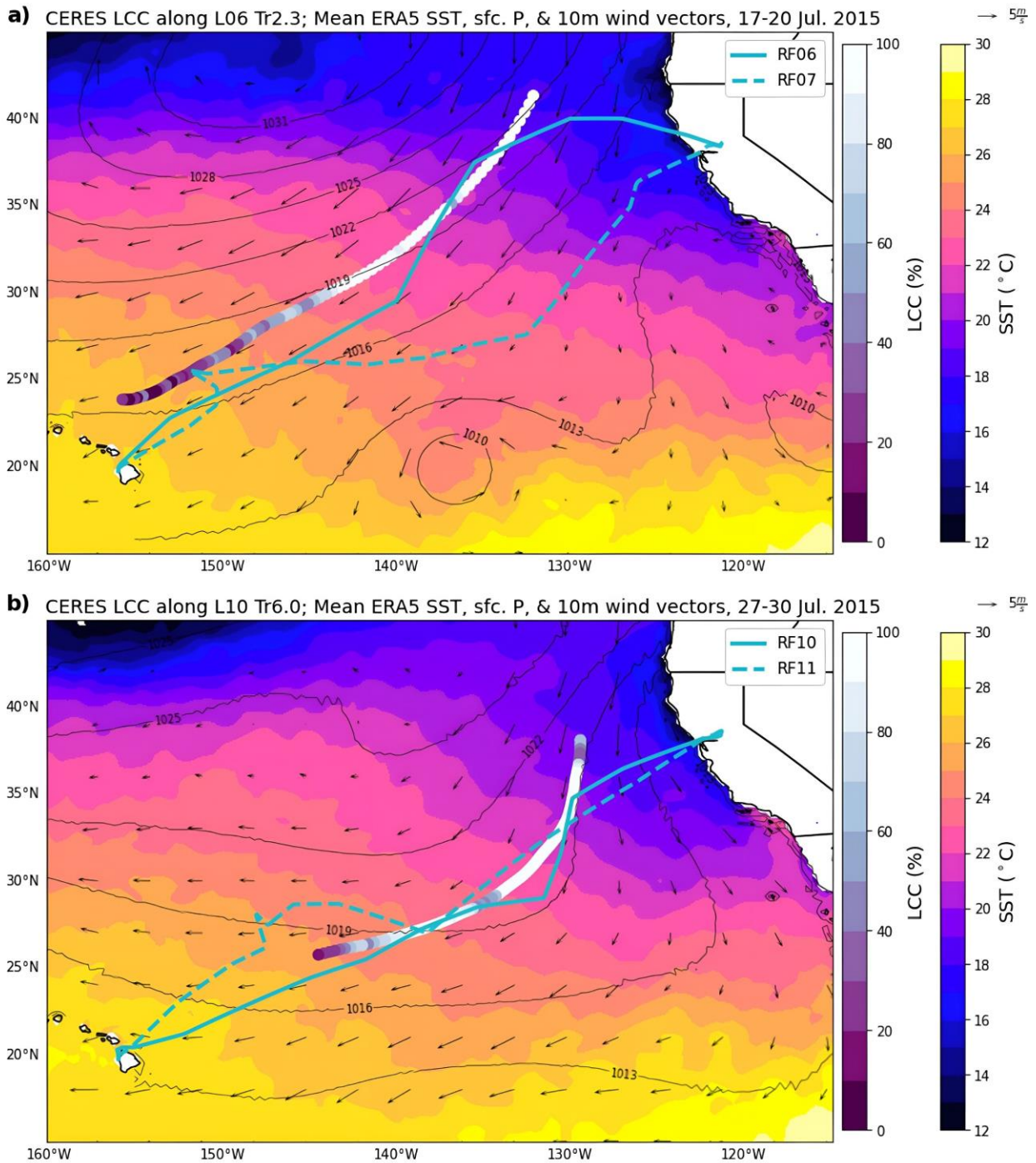


Figure 1. Selected CSET Lagrangian trajectories (filled markers) and flight paths (westward solid cyan lines, eastward dashed cyan lines) for the a) L06 and b) L10 cases used in this study. The filled markers' shades show the evolution in CERES low cloud cover along the trajectories. In the background map, shaded contours, black contours, and vectors show the ERA5 SST, surface pressure, and 10m wind speed, respectively, averaged for the periods a) 17-20 July 2015 and b) 27-30 July 2015.

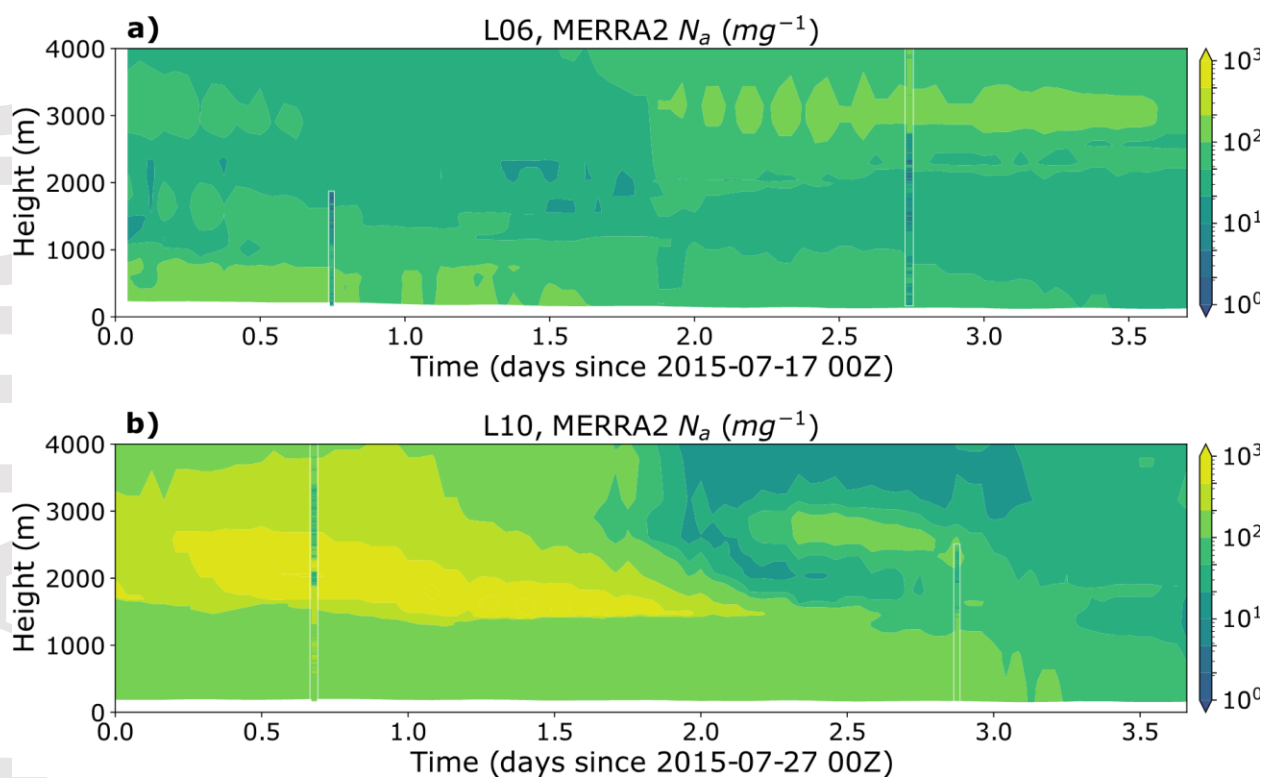


Figure 2. Time-height evolution of corrected MERRA2 N_a for the a) L06 and b) L10 cases. The superimposed thin vertical rectangles at about days 0.75 and 2.75 show the aircraft measurements of N_a for reference.

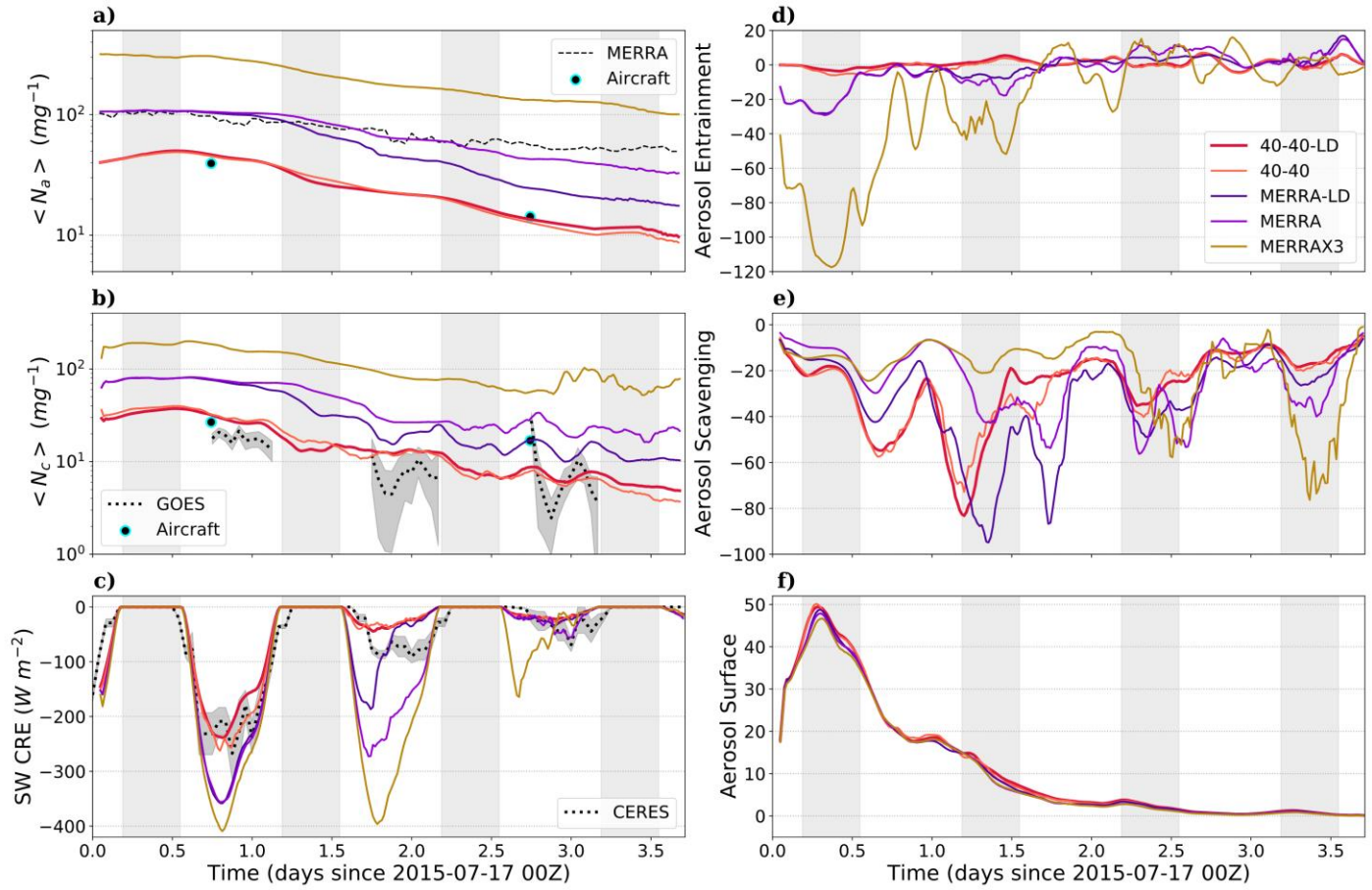


Figure 3. Left panels: time series for L06 of observed and modeled domain-averaged a) MBL-average total aerosol number concentration ($\langle N_a \rangle$), b) MBL-average cloud droplet number concentration ($\langle N_c \rangle$), and c) the shortwave cloud radiative effect (SW CRE, calculated as the all-sky minus clear-sky net SW at TOA). Right panels: select MBL-average aerosol budget tendencies for N_a due to d) cloud-top entrainment of lower FT air, e) MBL-averaged scavenging, and f) surface fluxes in units of $\text{mg}^{-1} \text{ day}^{-1}$. The light gray boxes show the nighttime periods.

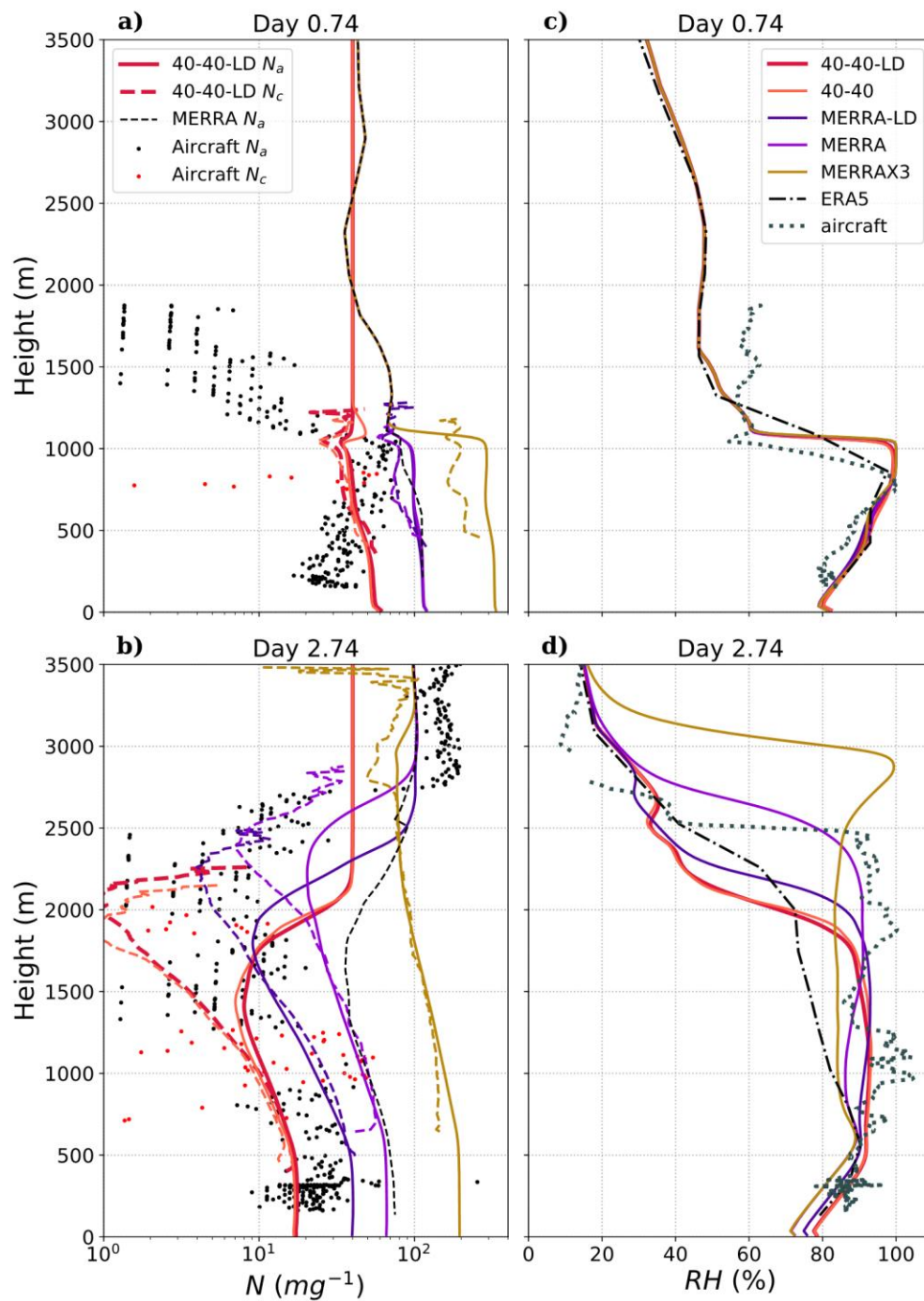


Figure 4. Vertical profiles of the observed and modeled domain-averaged N_a and N_c at the time of the a) westward and b) return flight observations for the L06 case. c&d) as in (a&b), but for relative humidity (RH).

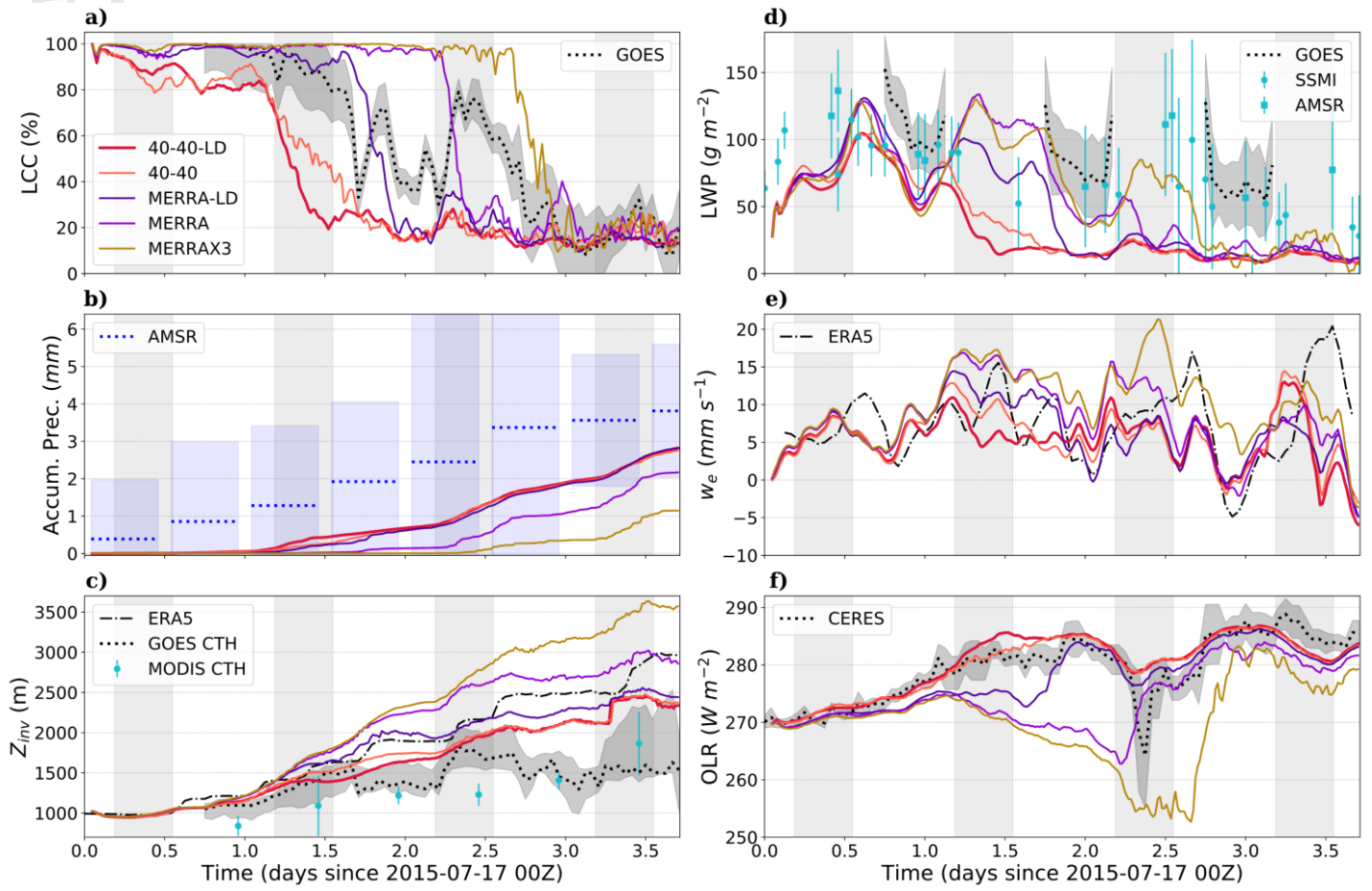


Figure 5. Macrophysical cloud properties for the L06 case from the simulations and observations. Time series of domain-averaged a) low cloud cover (LCC), b) accumulated precipitation, c) inversion height (Z_{inv}), d) cloud liquid water path (LWP), e) entrainment rate (w_e), and f) outgoing longwave radiation (OLR). The light gray boxes show the nighttime periods.

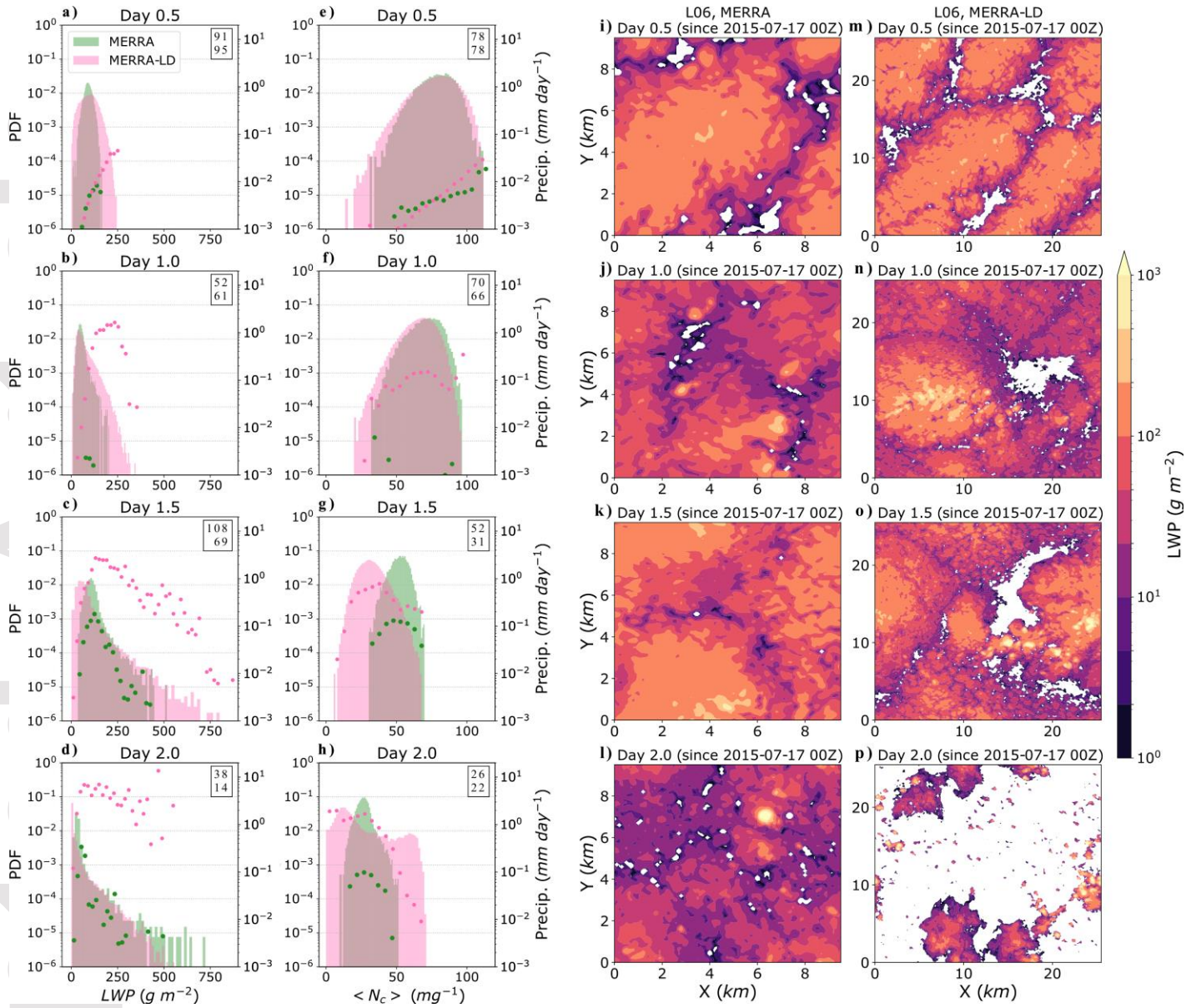


Figure 6. a-d) Probability distribution functions of cloud LWP at four times for L06, MERRA and MERRA-LD runs. The dots show precipitation in bins of LWP, and the boxes on the upper-right corner of each panel show domain-averaged LWP for MERRA (first value) and MERRA-LD (second value). Each panel shows data averaged for a period of 1 hour. e-h) as in a-d, but for $\langle N_c \rangle$. i-l) Snapshots of cloud LWP at four times for MERRA run. m-p) as in i-l, but for MERRA-LD run.

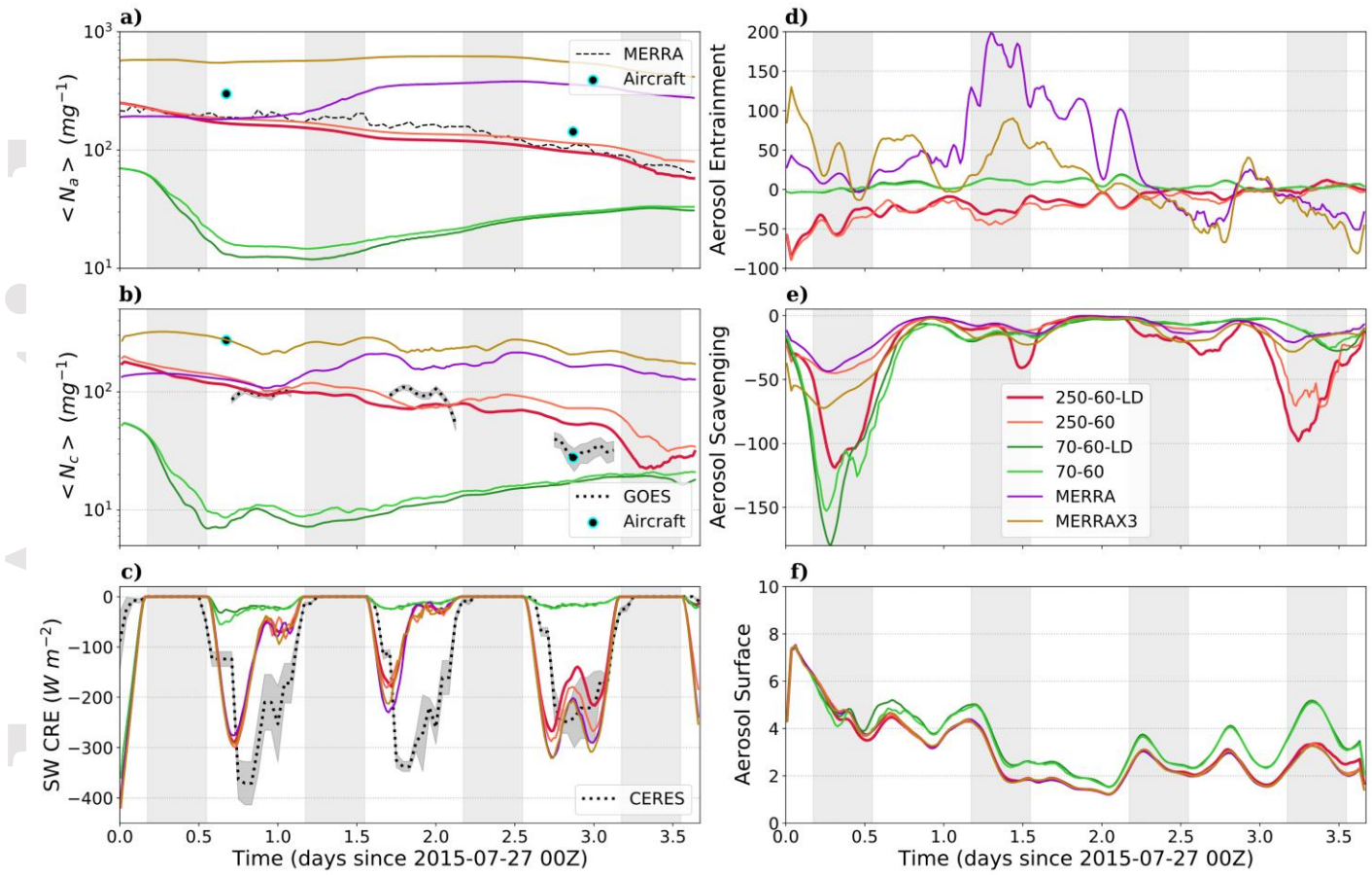


Figure 7. As in Figure 3, but for the L10 case.

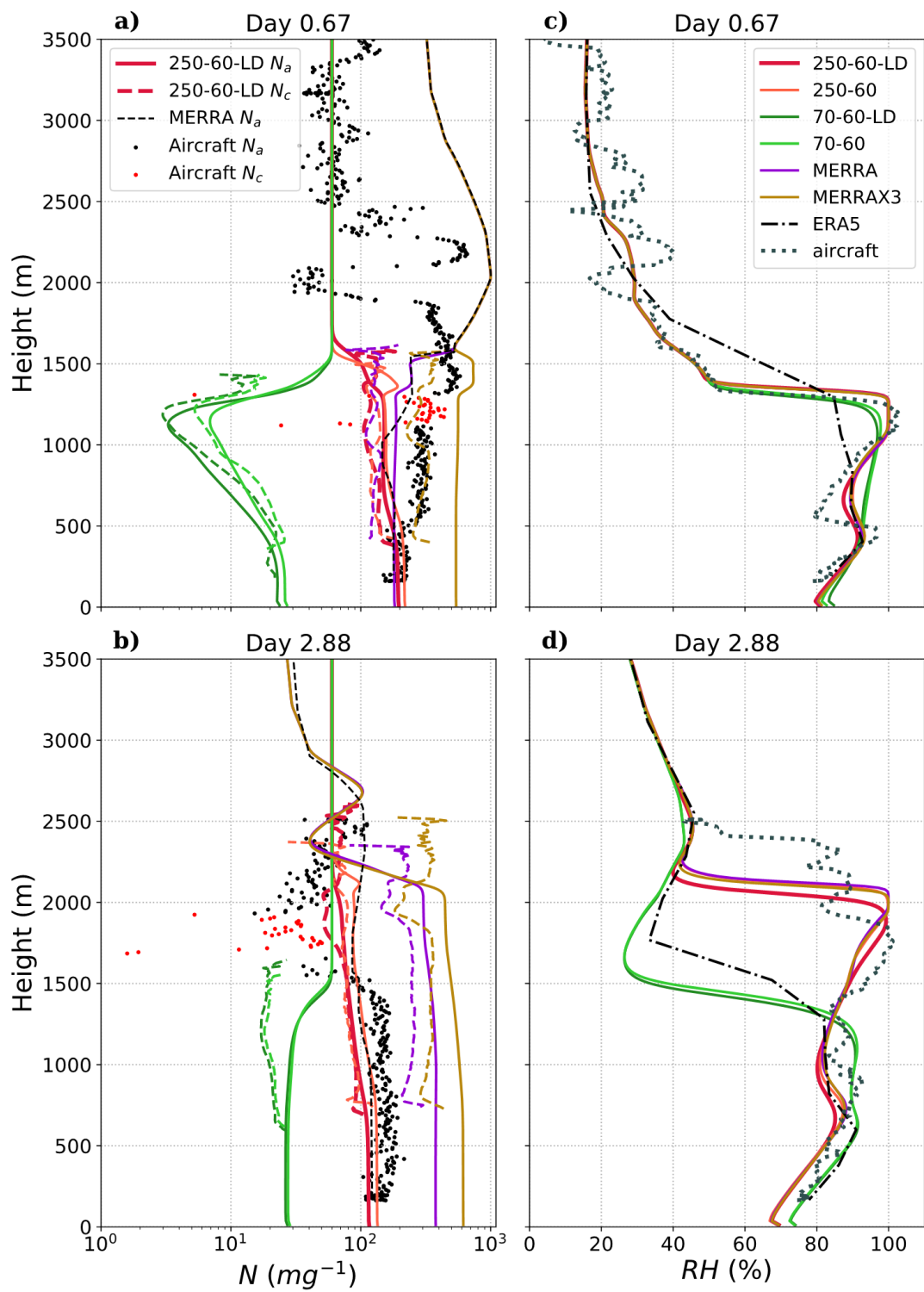


Figure 8. As in Figure 4, but for the L10 case.

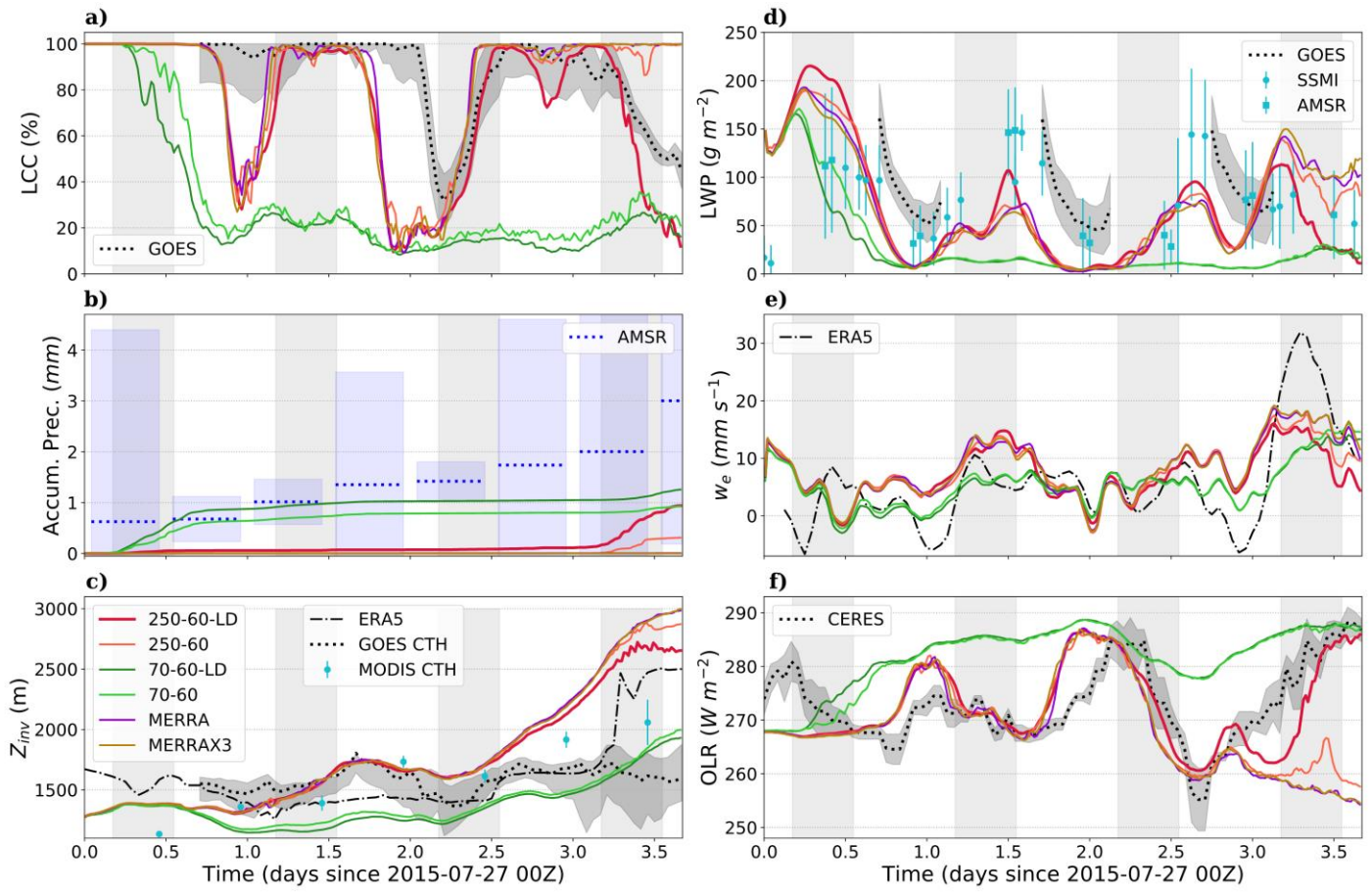


Figure 9. As in Figure 5, but for the L10 case.

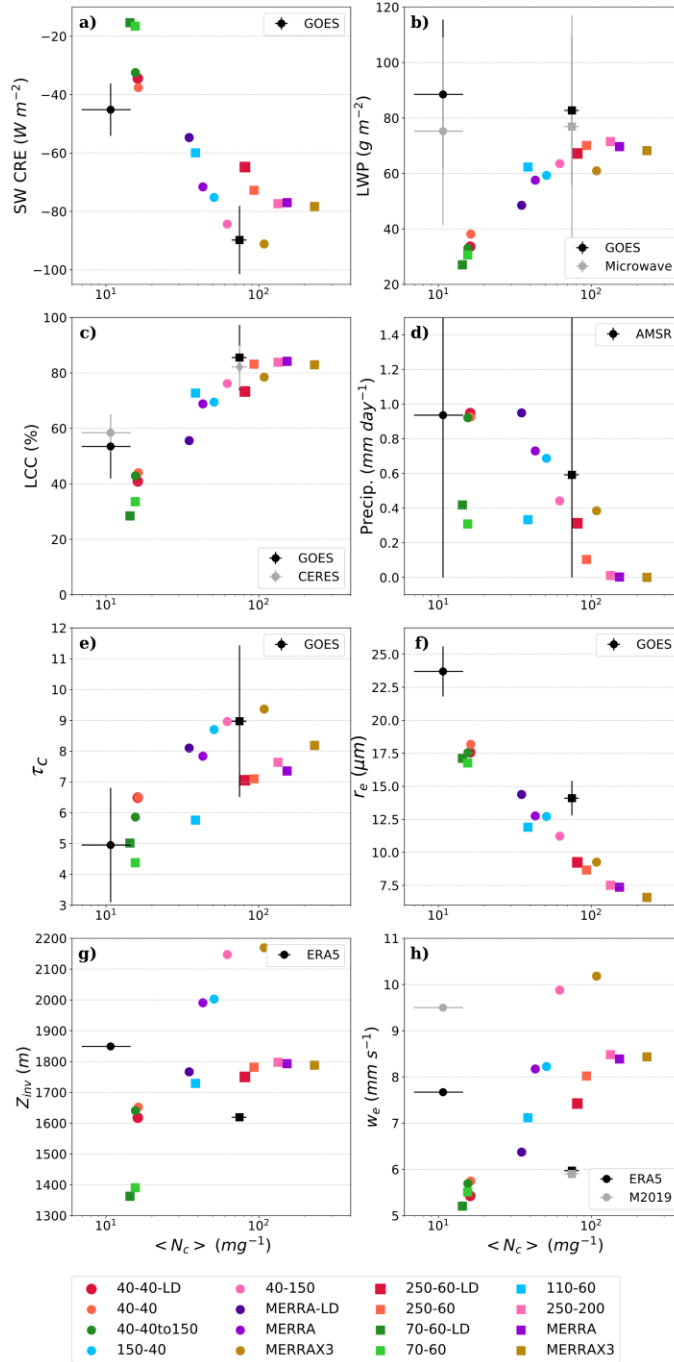


Figure 10. Microphysical and macrophysical variables as a function of $\langle N_c \rangle$ for the L06 (circles) and L10 (squares) cases, from both the simulations and selected observations. Variables on the y-axis are a) the short-wave cloud radiative effect (SW CRE), b) cloud LWP, c) LCC, d) surface precipitation, e) τ_c , f) r_e , g) Z_{inv} , and h) w_e . Each colored point shows results for one LES run averaged over the whole day-time period of the run. Observed values are plotted as black or gray circles for L06 and black or gray squares for L10 case. Here, the observed values of $\langle N_c \rangle$ are from GOES and the observed or reanalysis values of parameters are from sources as given in the upper-right corner of each panel.

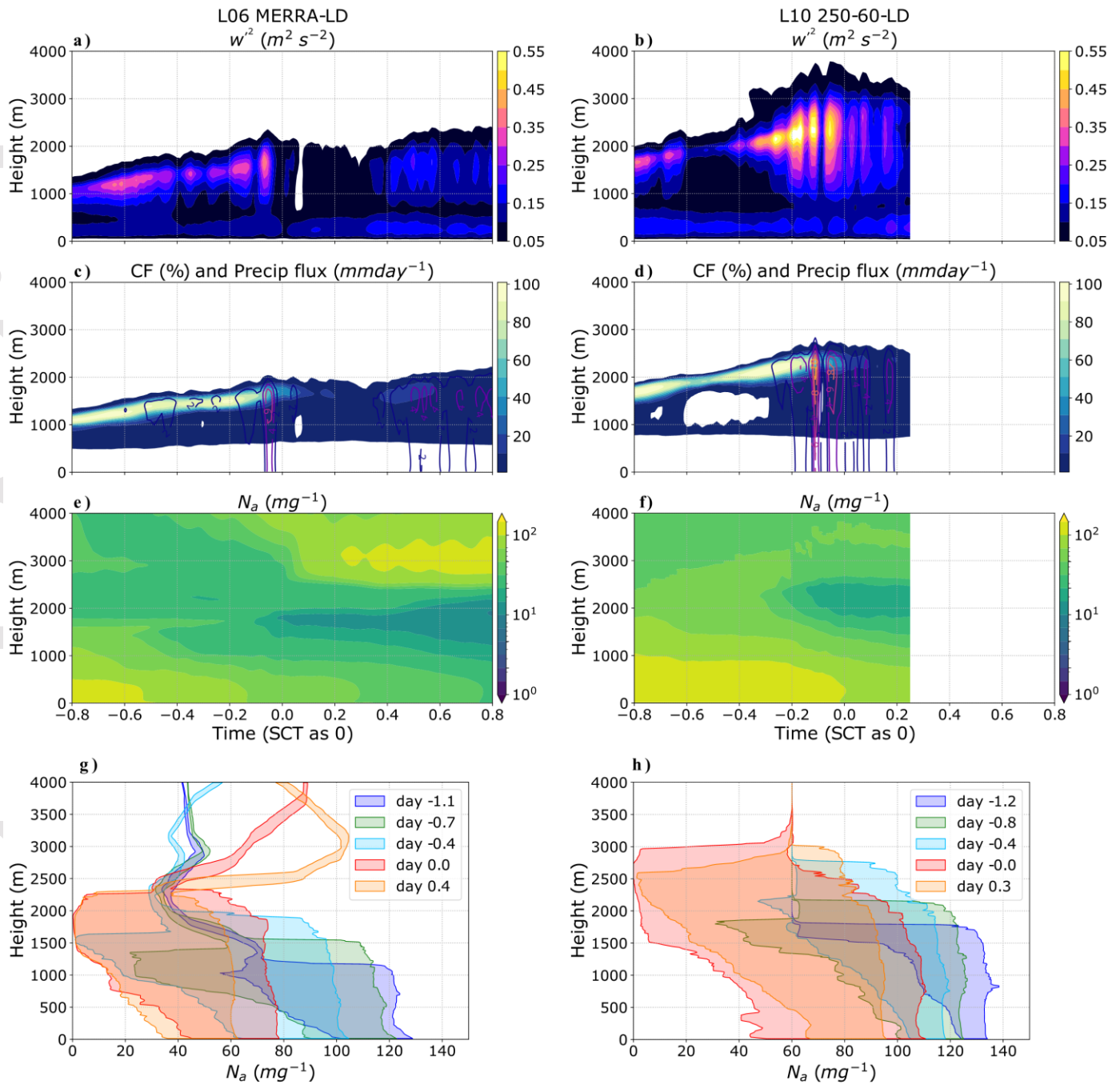


Figure 11. Time-height evolution of a&b) w'^2 , c&d) cloud fraction (CF) and precipitation flux, and e&f) N_a . The x-axis is time in fraction of a day relative to the time of the SCT. G&h) The vertical profiles of N_a are shown at several times near the time of the SCT. For each time, the shaded area between the two lines shows the 5th and 95th percentile range in the variable's probability distribution function (PDF). The results are for two LES runs: L06 MERRA-LD (left panels) and L10 250-60-LD (right panels).

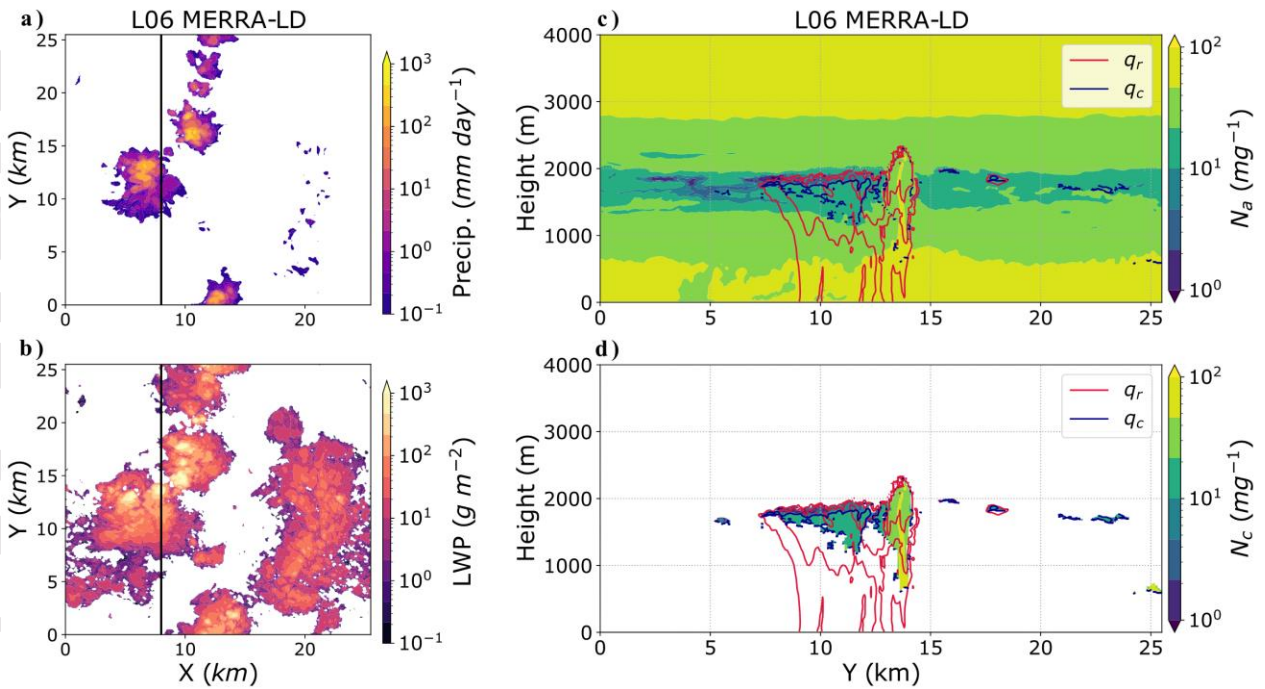


Figure 12. Left panels: snapshots of a) surface precipitation, and b) cloud LWP for the L06 MERRA-LD run at a time close to the SCT, day 1.875 (relative to the run start). Right panels: y-z cross-sections of c) N_a and d) N_c , with contours of rain mass or q_r ($1\text{e-}4$, $1\text{e-}3$ kg kg^{-1}) and cloud liquid mass or q_c ($1\text{e-}5$, $1\text{e-}4$, $1\text{e-}3$ kg kg^{-1}). Cross-sections are at $x = 8$ km (black lines in the left panels).

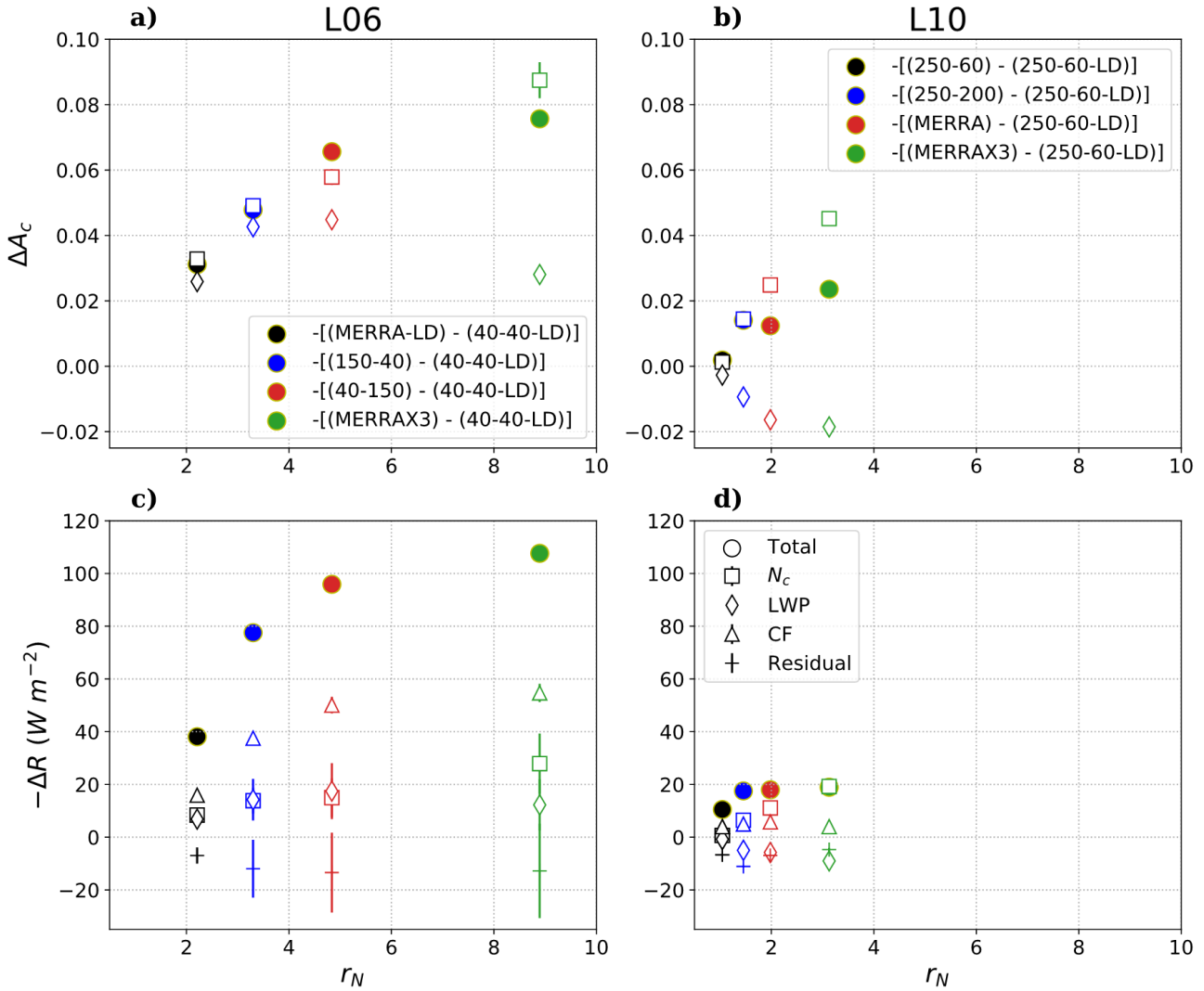


Figure 13. Upper panels: change in cloudy-sky albedo (ΔA_c) as a function of the ratio of the perturbed to baseline cloud droplet number concentration ($r_N = \frac{N_{c2}}{N_{c1}}$) for a) L06 and b) L10. Lower panels: change in the cloud radiative effect (ΔR) as a function of r_N for c) L06 and d) L10. Each point shows the variables for a pair of LES runs with values averaged over the whole day-time period of the run. The filled circles show the total change in A_c and R between the two LES runs. The square, diamond, triangle, and plus markers, respectively, show the effects of changes in N_c , LWP, CF, and the residual (CDNC + LWP + CF - Total). The markers for N_c , LWP, CF, and residual show the results of step 3, whereas the endpoints of bars show steps 1 and 2 of the calculations described in the text.

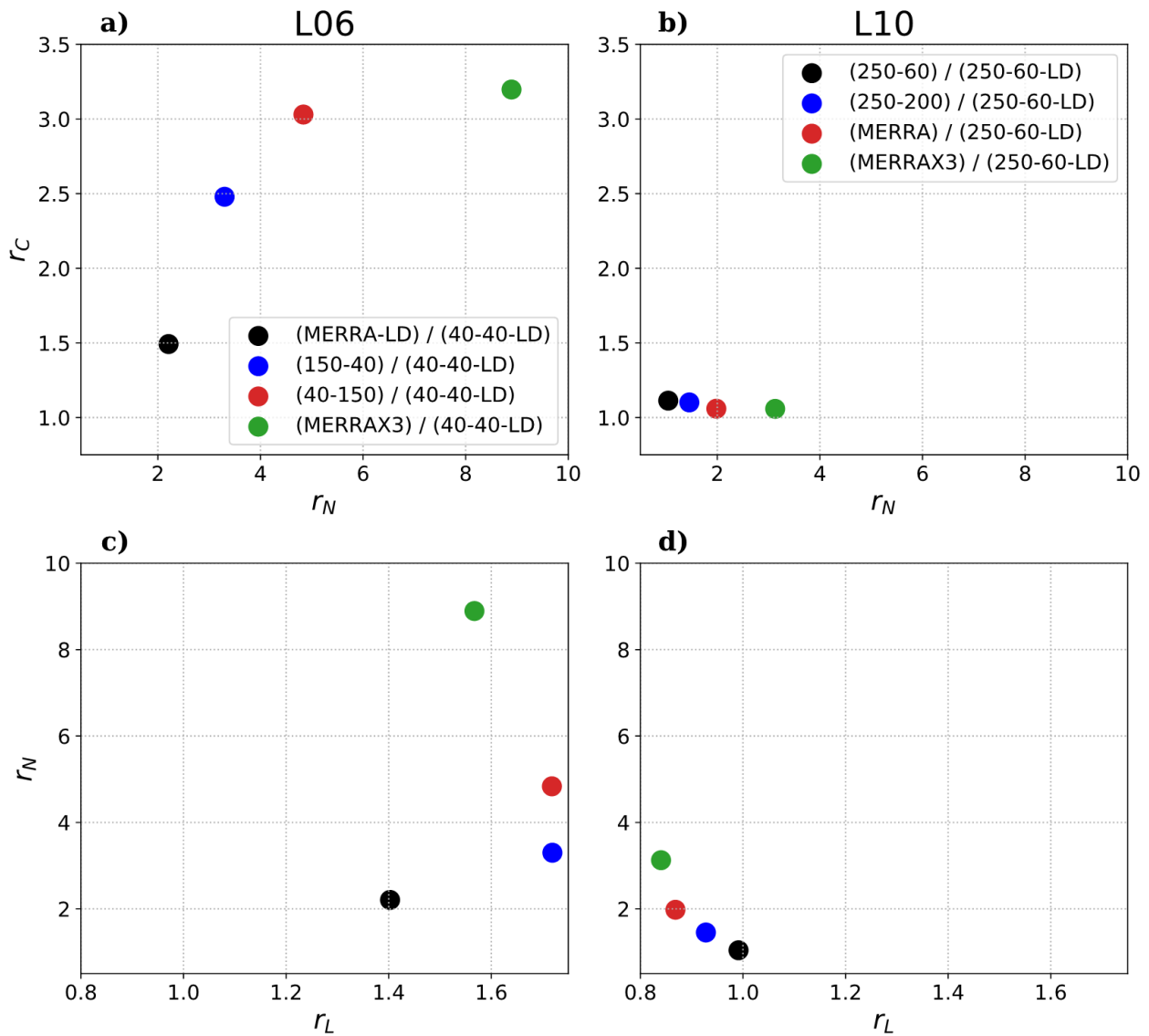


Figure 14. Upper panels: ratio of the perturbed to baseline cloud fraction ($r_c = \frac{c_2}{c_1}$) as a function of the ratio of the perturbed to baseline cloud droplet number concentration ($r_N = \frac{N_{c2}}{N_{c1}}$) for the a) L06 and b) L10 cases. Lower panels: r_N as a function of the ratio of the perturbed to baseline liquid water path ($r_L = \frac{L_2}{L_1}$) for the c) L06 and d) L10 cases. Each point shows the ratio between a pair of LES runs with values averaged over the whole day-time period of the run.

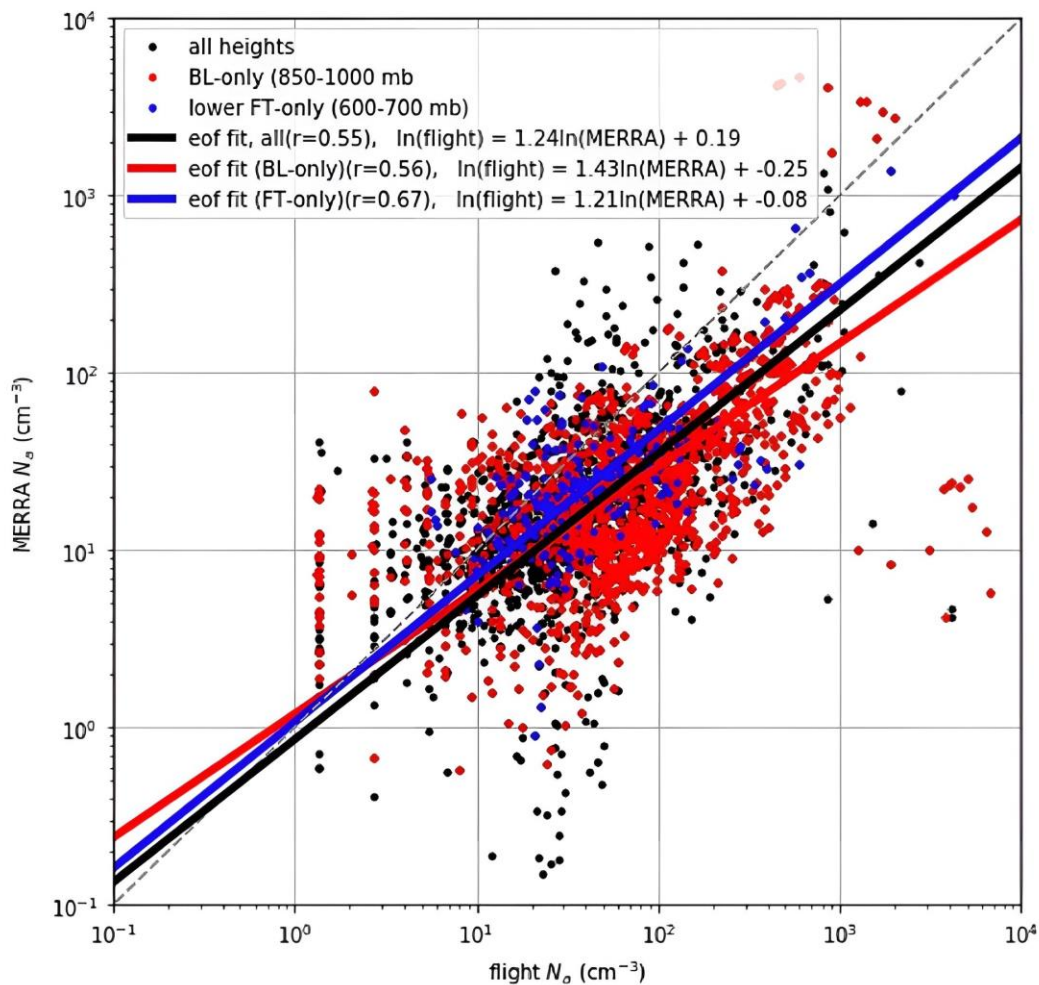


Figure A1. Linear regression in log-log space between N_a from all CSET flights and N_a derived from collocated MERRA2 data.